

Cover Page



Universiteit Leiden



The handle <http://hdl.handle.net/1887/36422> holds various files of this Leiden University dissertation.

**Author:** Díaz Morales, Oscar Alfonso

**Title:** Catalysis of the electrochemical water oxidation to oxygen

**Issue Date:** 2015-11-19

# List of publications

---

- O. Diaz-Morales, I. Ledezma-Yanez, M.T.M. Koper and F. Calle-Vallejo, “Guidelines for the rational design of Ni-based double hydroxide electrocatalysts for the oxygen evolution reaction”, *ACS Catal.* 2015, 5, 5380-5387
- I. Ledezma-Yanez, O. Diaz-Morales, M. Figueiredo, M.T.M. Koper, “Hydrogen Oxidation and Hydrogen Evolution on a Platinum Electrode in Acetonitrile”, *ChemElectroChem* 2015, DOI: 10.1002/celec.201500341.
- J. Shen, R. Kortlever, R. Kas, Y. Birdja, O. Diaz-Morales, Y. Kwon, I. Ledezma-Yanez, K. J. P. Schouten, G. Mul and M.T.M. Koper, “Electrocatalytic reduction of carbon dioxide to carbon monoxide and methane at an immobilized cobalt protoporphyrin in aqueous solution”, *Nat. Comm.* 2015, 6, 8177.
- F. Calle-Vallejo, O. Diaz-Morales, M. Kolb and M.T.M. Koper, “Why Is Bulk Thermochemistry a Good Descriptor for the Electrocatalytic Activity of Transition Metal Oxides?”, *ACS Catal.* 2015, 5, 869-873.
- O. Diaz-Morales, T.J.P. Hersbach, D.G.H. Hetterscheid, J.N.H. Reek and M.T.M. Koper, “Electrochemical and Spectroelectrochemical Characterization of an Iridium-Based Molecular Catalyst for Water Splitting: Turnover Frequencies, Stability, and Electrolyte Effects”, *J. Am. Chem. Soc.* 2014, 136, 10432-10439.
- O. Diaz-Morales, F. Calle-Vallejo, C. de Munck and M.T.M. Koper, “Electrochemical water splitting by gold: evidence for an oxide decomposition mechanism”, *Chem. Sci.*, 2013, 4, 2334-2343. (**Front cover of Issue**)

- O. Diaz-Morales, J. Mostany, C. Borrás, B.R. Scharifker, “Current transient study of the kinetics of nucleation and diffusion-controlled growth of bimetallic phases”, *J. Solid State Electrochem.* 2013, 17, 345-351.

# Curriculum Vitae

---

Oscar was born in Caracas, Venezuela on the 26<sup>th</sup> of September 1984. After high school, he studied Chemistry at Simón Bolívar University (USB), and finished his bachelor in 2008 with a research thesis on “Heavy metal detection by anodic stripping voltammetry in closed loop flow systems”. He continued at USB for his master’s degree in Chemistry under the supervision of Prof. Dr. Benjamin Scharifker, studying the electrodeposition of bimetallic alloys; the topic of his master research was “Electrochemical bimetallic phase formation”. In 2009, he did an internship at the Institute of Physical Chemistry “Rocasolano” under the supervision of Dr. Angel Cuesta, studying the alloy formation process during the underpotential metal deposition by means of potential-modulated ultraviolet spectroscopy; the internship was funded by a fellowship awarded by the Venezuelan Research Council. He obtained his master’s degree (with honors) in 2011.

In June 2011, Oscar started his PhD work in Leiden University (the Netherlands) under the supervision of Prof. Dr. Marc T. M. Koper with the project title of “Catalysis of the electrochemical water oxidation to oxygen” sponsored by the BioSolar Cell open innovation consortium, to understand the parameters affecting the electrochemical oxygen evolution reaction. The results of this work are presented in this thesis; parts of his work have been presented at several international conferences.



## Appendix A: Supplementary Material for Chapter 2

### *Evidences for Gold Oxide Decomposition Mechanism during the Electrochemical Water Oxidation*

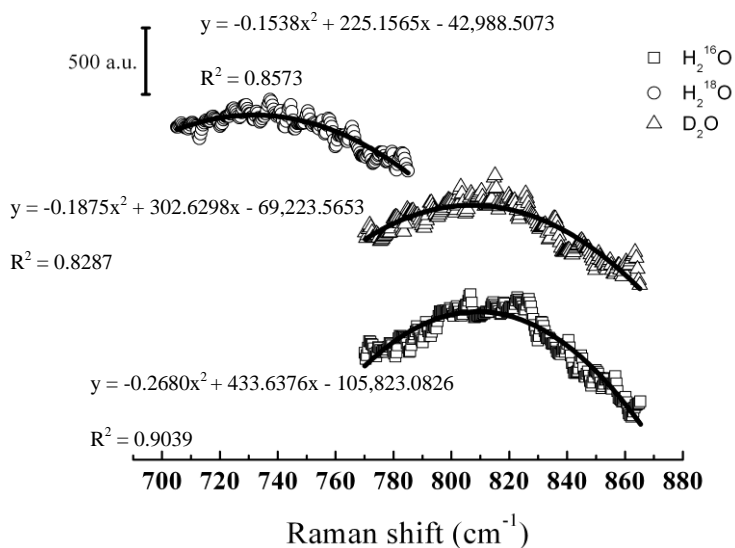


**Figure A1.** Raman spectrum acquired at 1.7 V vs. RHE in a pH=0 solution prepared with H<sub>2</sub><sup>16</sup>O, H<sub>2</sub><sup>18</sup>O and D<sub>2</sub>O, showing the polynomial fittings (second grade polynomial) used to determine the peak position.

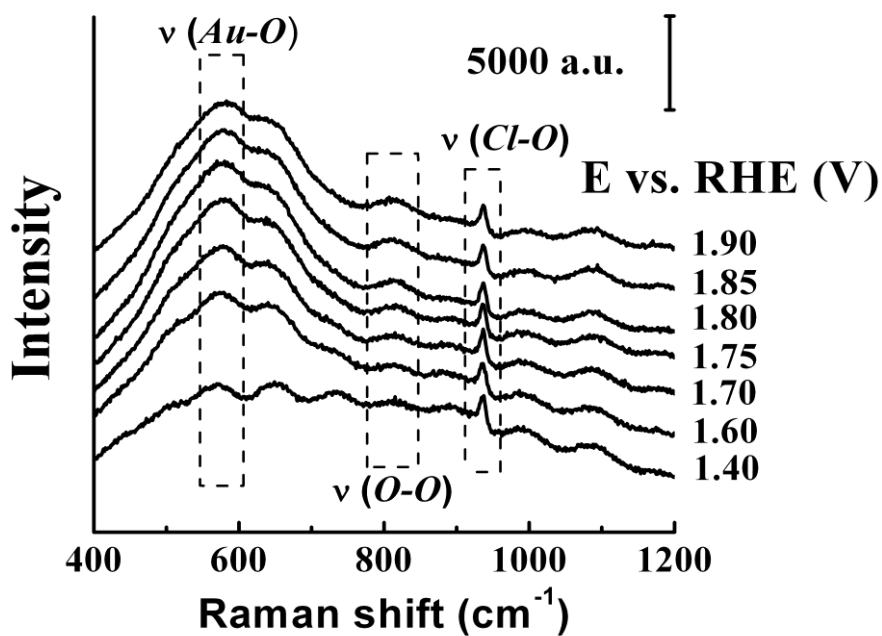
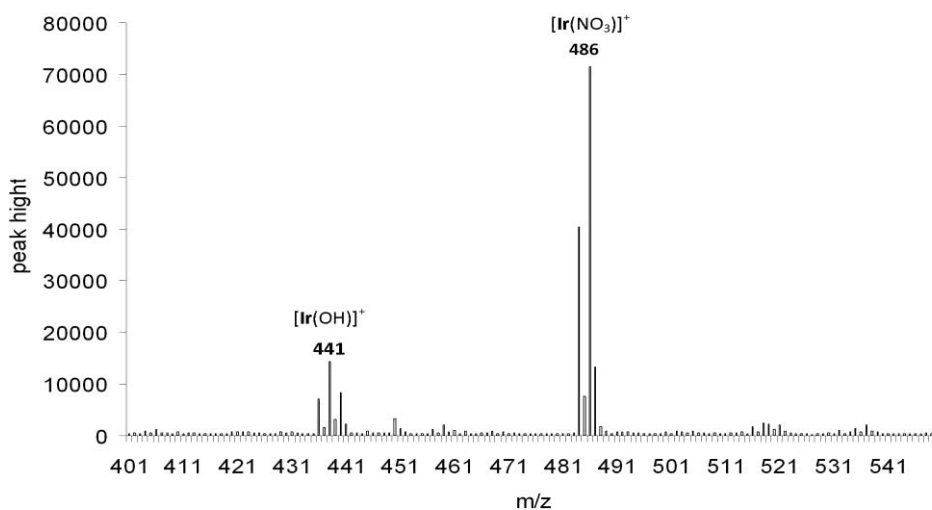


Figure A2. SERS spectra for oxygen evolution acquired at constant potential in pH=0 solution prepared in D<sub>2</sub>O.

## Appendix B: Supplementary Material for Chapter 3

*Electrochemical and Spectroelectrochemical Characterization of an Iridium-based Molecular Catalyst for Oxygen evolution: Turnover Frequencies, Stability and Electrolyte Effects*



**Figure B1.** ESI-MS spectrum of  $\text{Ir}(\text{OH})_2$  at pH 1 when acidified with  $\text{HNO}_3$ . An identical ESI-MS spectrum is obtained upon dissolving  $[\text{Ir}(\text{NO}_3)_2]$  in water.



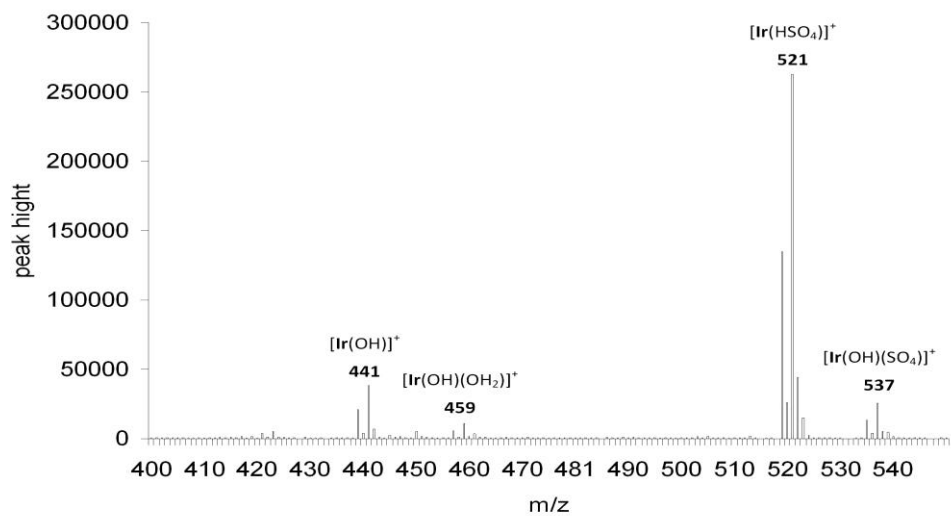


**Figure B2.** ESI-MS spectrum of  $\text{Ir}(\text{OH})_2$  at pH 1 when acidified with  $\text{H}_2\text{SO}_4$ .

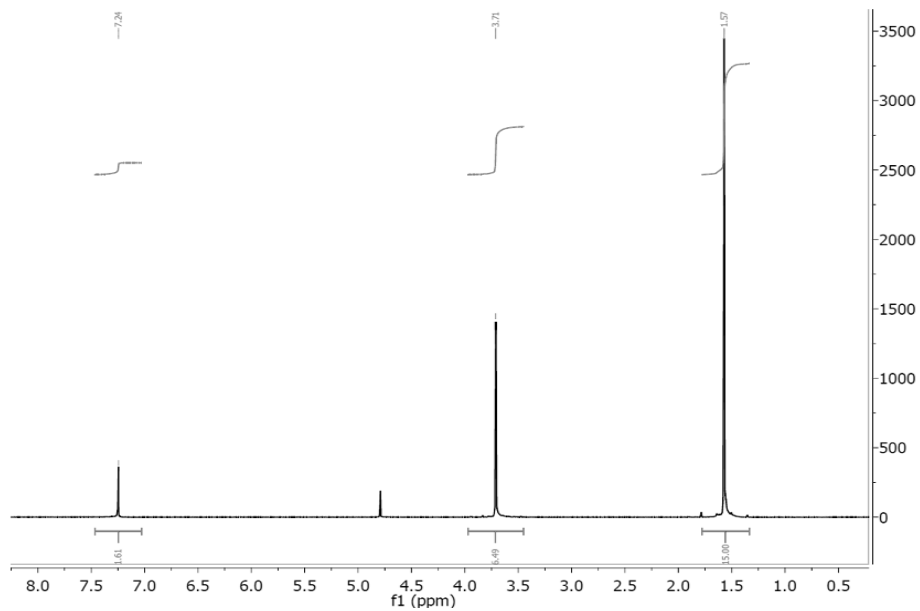


**Figure B3.**  $^1\text{H}$  NMR spectrum of iridium-N-dimethylimidazolin-2-ylidene in  $\text{D}_2\text{O}$  at pH 1.

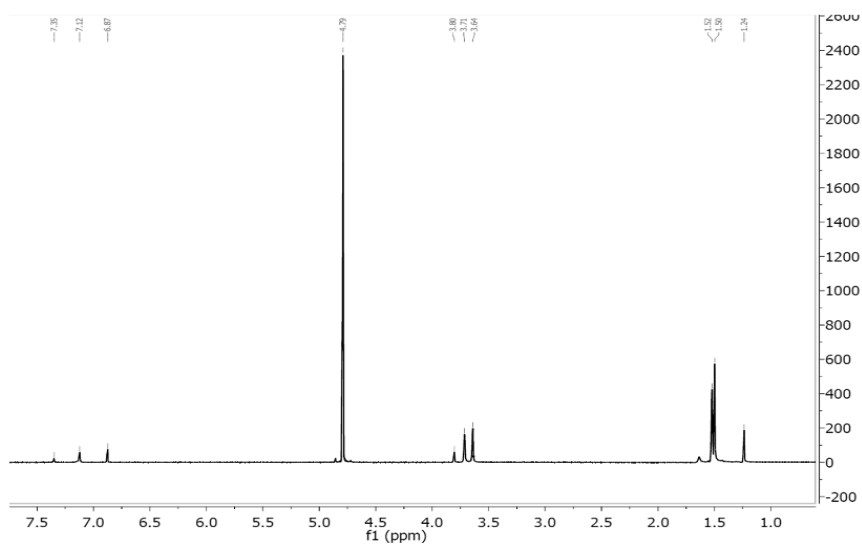


**Figure B4.** <sup>1</sup>H NMR spectrum of iridium-N-dimethylimidazolin-2-ylidene in D<sub>2</sub>O at pH 7.

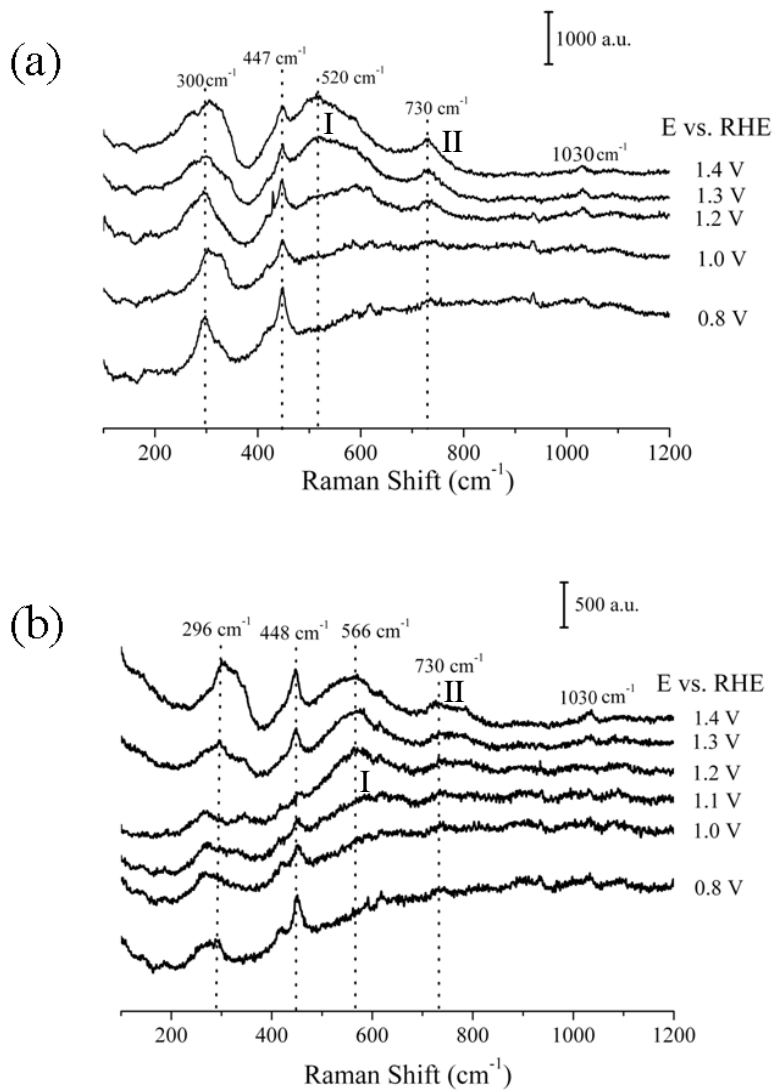


**Figure B5.** SERS spectra of the Ir-based molecular catalyst drop casted on gold, acquired in potentiostatic conditions in 0.1 M  $\text{HClO}_4$ : (a) measured in  $^{18}\text{O}$  water, (b) measured in  $\text{D}_2\text{O}$ .

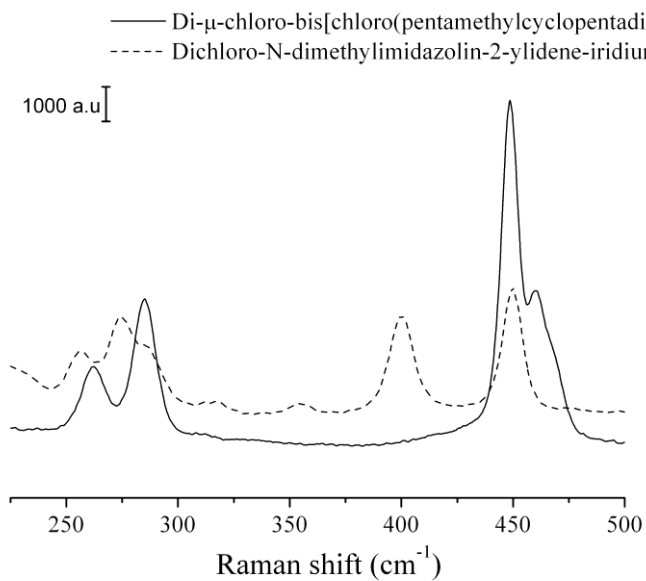


**Figure B6.** Spectra for Di-μ-chloro-bis[chloro(pentamethylcyclopentadienyl)iridium(III)], and Di-chloro-N-dimethylimidazolin-2-ylidene-pentamethylcyclopentadienyl)iridium(III) acquired in normal Raman mode

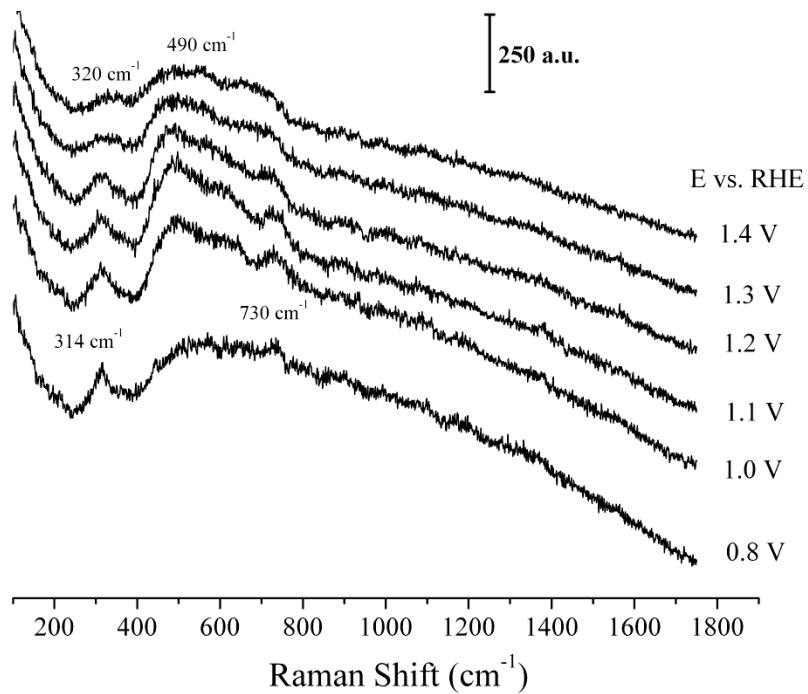


**Figure B7.** SERS spectra of iridium oxide nanoparticles drop-casted on gold, acquired under potentiostatic conditions in 0.1 M  $\text{HClO}_4$ .

**Table B1.** Position and error of the Raman the peak I and II (see Figure 5 in discussion) in the three media studied and ratio between the position of the peaks in  $^{18}\text{OH}_2$  and  $\text{D}_2\text{O}$  versus  $^{16}\text{OH}_2$ . Average obtained out of three different measurements.

	<b>Peak I position (<math>\text{cm}^{-1}</math>)</b>	<b>Peak II position (<math>\text{cm}^{-1}</math>)</b>	<b>Ratio <math>^{18}\text{O}/^{16}\text{O}</math> and D/H</b>
$^{16}\text{OH}_2$	$564 \pm 8$	$733 \pm 7$	-----
$^{18}\text{OH}_2$	$537 \pm 5$	$725 \pm 5$	0.95
$^{16}\text{OD}_2$	$565 \pm 4$	$732 \pm 6$	1.00

## Appendix C: Supplementary Material for Chapter 4

### *Guidelines for the Rational Design of Nickel-based Double Hydroxide Electrocatalysts for the Oxygen Evolution Reaction*

#### X-Ray Diffraction data

The XRDs were analyzed with X'Pert HighScore 2.0.1. The pattern for the product of thermal decomposition of NiFe DH fits well with the pattern number 00-044-1485 corresponding to  $\text{NiFe}_2\text{O}_4$ , see Figure C1. The XRD of pristine NiFe DH shows a compound of low crystallinity and the phase analysis was not possible. However, the segregation of  $\text{Ni}(\text{OH})_2$  was discarded upon comparison with the XRD of the double hydroxide with the pattern of  $\text{Ni}(\text{OH})_2$ , as shown in Figure C2. Thus, there are no significant evidences of pure  $\text{Ni}(\text{OH})_2$  formation.

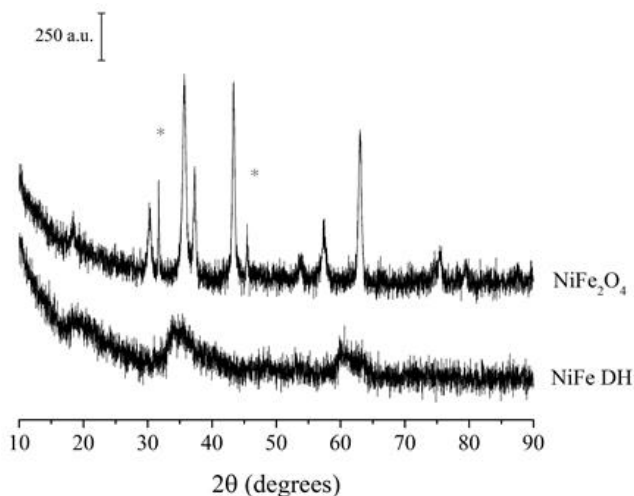


**Figure C1.** Powder XRD of the (as prepared) NiFe DH and  $\text{NiFe}_2\text{O}_4$  (product of thermal decomposition of the DH at 600 °C). The stars mark the peaks belonging to a second, unknown phase formed in small amounts during the thermal decomposition of NiFe DH.



The analysis of the XRD of NiMn DH with X'Pert HighScore 2.0.1 confirmed that manganese precipitated as manganese carbonate. The XRD of the double hydroxide fits well with the pattern number 00-007-0268 of  $\text{MnCO}_3$  (the peaks corresponding to this phase are marked with orange stars in Figure C3).

The XRD of the NiCo DH indicates the formation of a separate phase of pure  $\text{Ni}(\text{OH})_2$  (the peaks corresponding to this phase are marked with black stars in Figure C2).

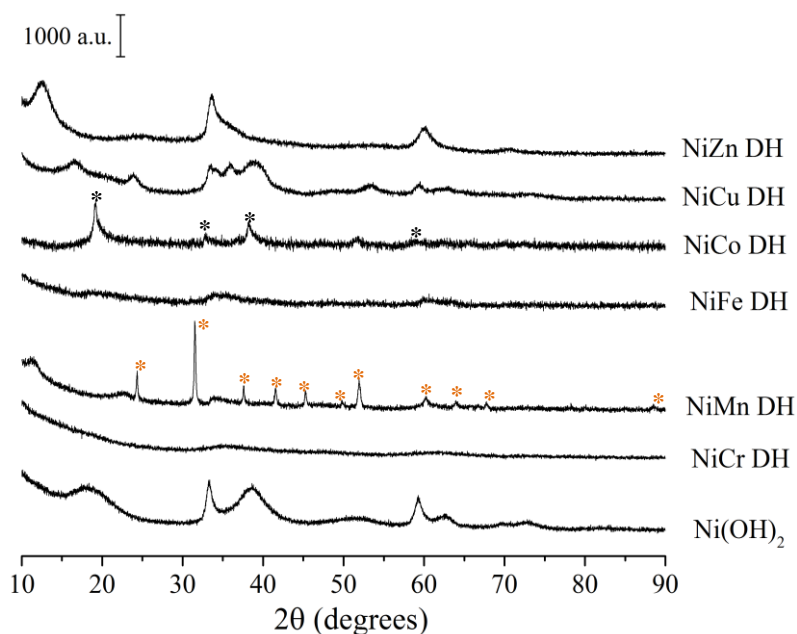


**Figure C2.** Powder XRDs of the Ni-based DHs with various transition metals. The XRD pattern of  $\text{Ni}(\text{OH})_2$  is also presented for comparison. The black stars indicate the peaks corresponding to pure  $\text{Ni}(\text{OH})_2$  in NiCo DH, while the orange stars indicate the peaks corresponding to  $\text{MnCO}_3$  in NiMn DH.

### Effect of Fe doping on the catalytic activity of NiFe DH

NiFe DH with Fe content in the range 25-75% was synthesized to assess doping effects in the catalytic activity. Figure C3 summarizes the results obtained for this experiment, in which it is clear that the highest catalytic activity is reached for 50 % Fe doping.

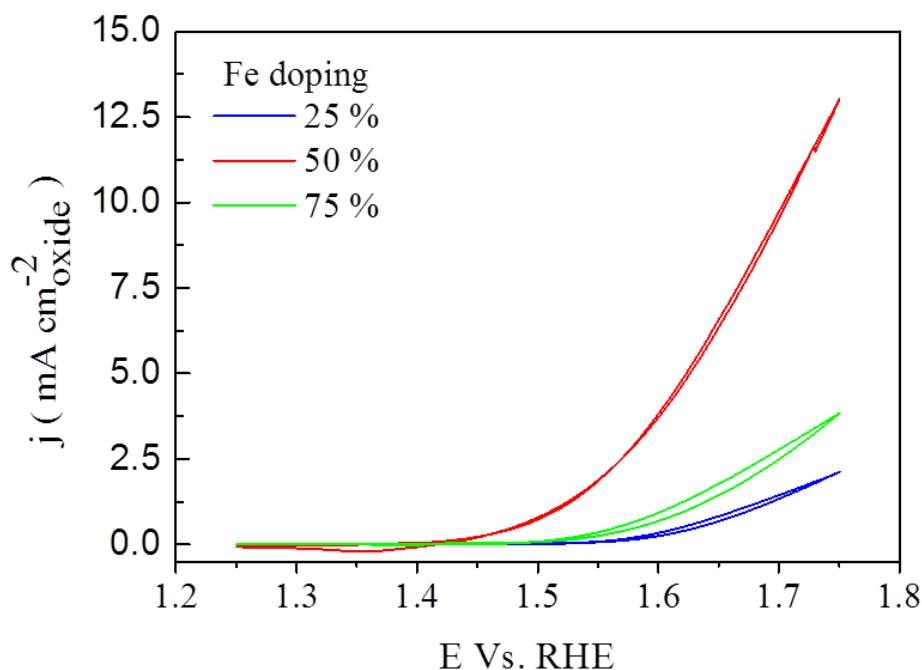


**Figure C3.** Cyclic voltammety for oxygen evolution in 0.1 M KOH for NiFe DH with different percentages of Fe doping. The NiFe DH was immobilized on Au. The experiments were performed under hydrodynamic conditions (rotation rate: 1500 RPM, scan rate: 0.01 V s<sup>-1</sup>).

### Infrared data

Figure C4 shows the infrared spectra for the different DHs. The first band (depicted in red) corresponds to the  $\nu_2$ -CO<sub>3</sub><sup>2-</sup> symmetric vibration,<sup>1-3</sup> and appears to be larger for the NiMn

DH. The next band at *ca.* 1080  $\text{cm}^{-1}$  (in blue), shows the  $\nu_1$  symmetric vibration from carbonate ion, which suggests a degeneration in the symmetry of the carbonate ion from  $D_{3h}$  a  $C_{2v}$ .<sup>1,2,4</sup> The green band around 1390  $\text{cm}^{-1}$  corresponds to the  $\nu_1$ - $\text{CO}_3^{2-}$  anti-symmetric vibration,<sup>5</sup> present in all samples, but appears broaden for the NiMn DH, confirming the presence of superficial and interstitial  $\text{MnCO}_3$ . We also observe the  $\nu_3$ - $\text{CO}_3^{2-}$  symmetric band at *ca.* 1530  $\text{cm}^{-1}$  (purple line) as well as the  $\delta$ -HOH around 1664  $\text{cm}^{-1}$  (brown line).<sup>1-4,6</sup> The former band indicates the presence of water in the first coordination sphere of the DHs. Meanwhile, NiMn and NiCo show a band around 3380  $\text{cm}^{-1}$  (in orange), corresponding to “free” water,<sup>5</sup> and it is an indicative for the presence of  $\text{Mn}(\text{H}_2\text{O})_x$  and  $\text{Co}(\text{H}_2\text{O})_x$  complexes and simple out-of-coordination-sphere hydration. The hydration water coordinated to the Ni is depicted in olive,<sup>3,6</sup> and appears at 3625  $\text{cm}^{-1}$ .

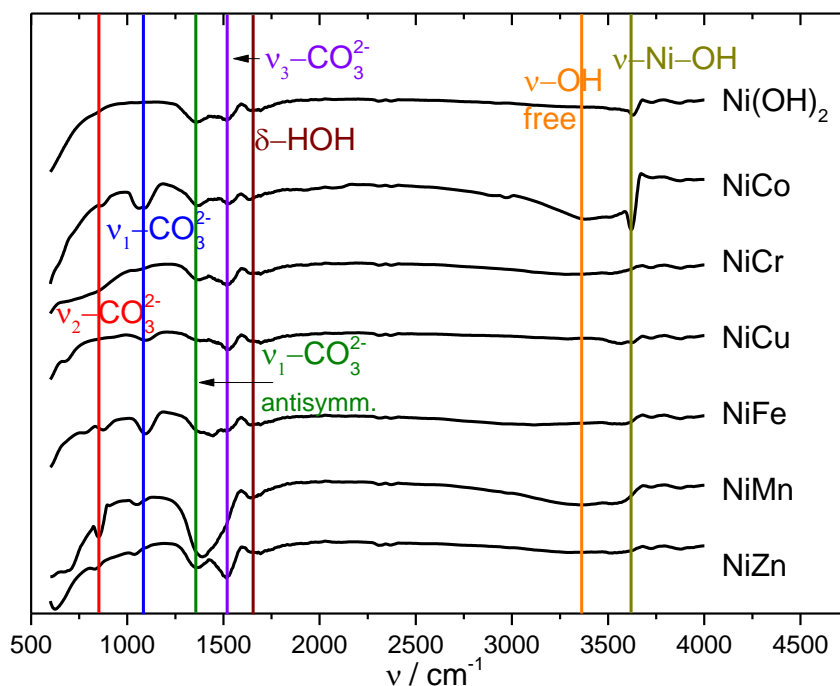


**Figure C4.** Infrared spectra for the Ni-based DHs with transition metals. The spectra are presented with the respective frequency assignment of the characteristic bands.

- (1) Frost, R. L.; Ding, Z.; Martens, W. N.; Johnson, T. E.; Kloprogge, J. T. *Spectrochimica Acta Part A: Molecular and Biomolecular Spectroscopy* **2003**, *59*, 321.
- (2) Frost, R. L.; Martens, W.; Ding, Z.; Kloprogge, J. T.; Johnson, T. E. *Spectrochimica Acta Part A: Molecular and Biomolecular Spectroscopy* **2003**, *59*, 291.
- (3) Kloprogge, J. T.; Frost, R. L. *J. Solid State Chem.* **1999**, *146*, 506.
- (4) Cochei, L.; Barvinschi, P.; Pode, R.; Popovici, E.; Seftel, E. M. *Chem. Bull. "POLITEHNICA" Univ. (Timisoara)* **2010**, *55*, 40.
- (5) Lambert, J. B. *Introduction to organic spectroscopy*; Macmillan: New York, 1987.
- (6) Frost, R. L.; Weier, M. L.; Clissold, M. E.; Williams, P. A. *Spectrochimica Acta Part A: Molecular and Biomolecular Spectroscopy* **2003**, *59*, 3313.

**Effect of the precipitating agent of NiCr, NiMn and NiFe DHs on their catalytic activity towards OER**

The effect of the precipitating agent used in the synthesis of NiCr, NiMn and NiFe DHs on their OER activity was assessed by replacing the sodium carbonate used in the synthesis for a solution 2 M NaOH, following the co-precipitation procedure described in section 4.2.4 of this work. Figure C5 compares the OER activity of the three nickel-based double hydroxide. It is clear from the plot that the precipitation with sodium carbonate (at constant pH) generates catalysts with higher OER activity than the procedure performed with sodium hydroxide.

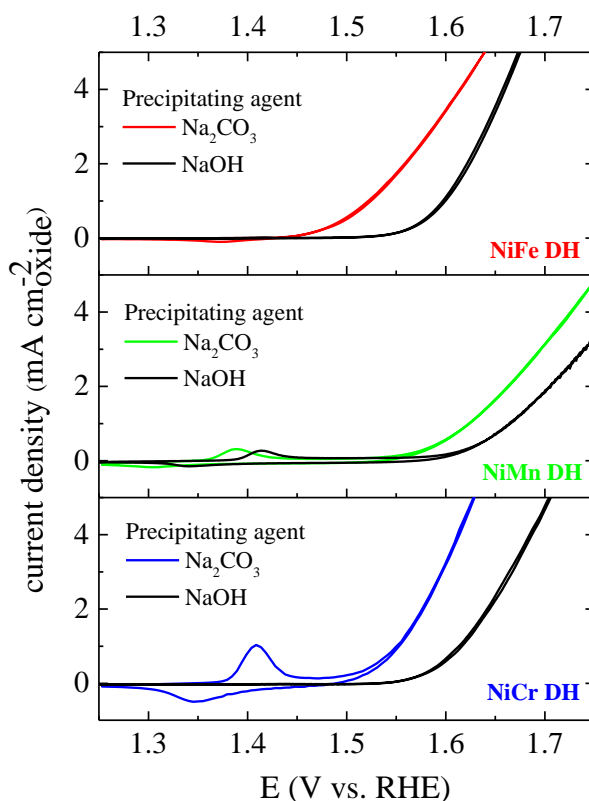


**Figure C5.** Effect of the precipitating agent during the synthesis of NiCr, NiMn and NiFe DHs on their catalytic activity towards the oxygen evolution reaction in 0.1 M KOH. The experiments were performed under hydrodynamic conditions (rotation rate: 1500 RPM, scan rate: 0.01 V s<sup>-1</sup>).

**Catalytic activity towards OER of NiFe DH in comparison with the IrO<sub>2</sub>**

The catalytic activity of the NiFe DH towards electrochemical water oxidation in alkaline media was compared with the activity measured on IrO<sub>2</sub>, reported as benchmark for the oxygen evolution reaction.<sup>1,2</sup> IrO<sub>2</sub> deposition was performed as reported in literature.<sup>3</sup> Figure C6 summarizes the results of these measurements, it is clear that NiFe DH reported in this work shows higher intrinsic catalytic activity (expressed as current density) towards oxygen evolution when it is compared with the benchmark IrO<sub>2</sub> catalyst.

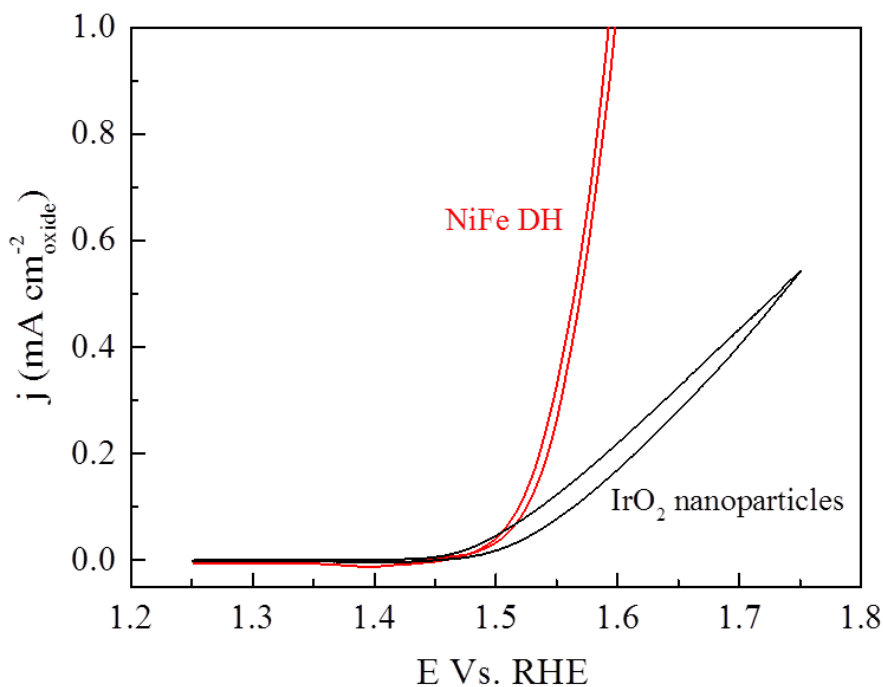


**Figure C6.** Polarization curve for the oxygen evolution reaction in 0.1 M KOH for NiFe DH and IrO<sub>2</sub> nanoparticles immobilized on Au. The experiments were performed under hydrodynamic conditions (rotation rate: 1500 RPM, scan rate: 0.01 V s<sup>-1</sup>).

**Stability of NiFe DHs under anodic conditions**

The stability of the NiFe DH electrocatalyst was assessed by galvanostatic electrolysis, using the approach reported by McCrory *et al.*<sup>2</sup> Figure C7a shows the evolution of the overpotential during an electrolysis carried out by applying a current density of  $10 \text{ mA cm}_{\text{disk}}^{-2}$  for 2 h. The overpotential at the beginning of the electrolysis is plotted versus the value measured after 2 h, and the results are shown in Figure C7b. The results reported by McCrory *et al.*<sup>2</sup> for the electrochemical water oxidation in NaOH 1 M on  $\text{IrO}_x$ ,  $\text{NiFeO}_x$  and NiO are presented for comparison. Note that the diagonal dashed line in Figure C7b represents the expected response of a stable catalyst. The results in Figure C7.a clearly show that NiFe DH is stable under anodic conditions, has activities comparable to those of  $\text{NiFeO}_x$  catalysts and is more stable than  $\text{IrO}_x$ .

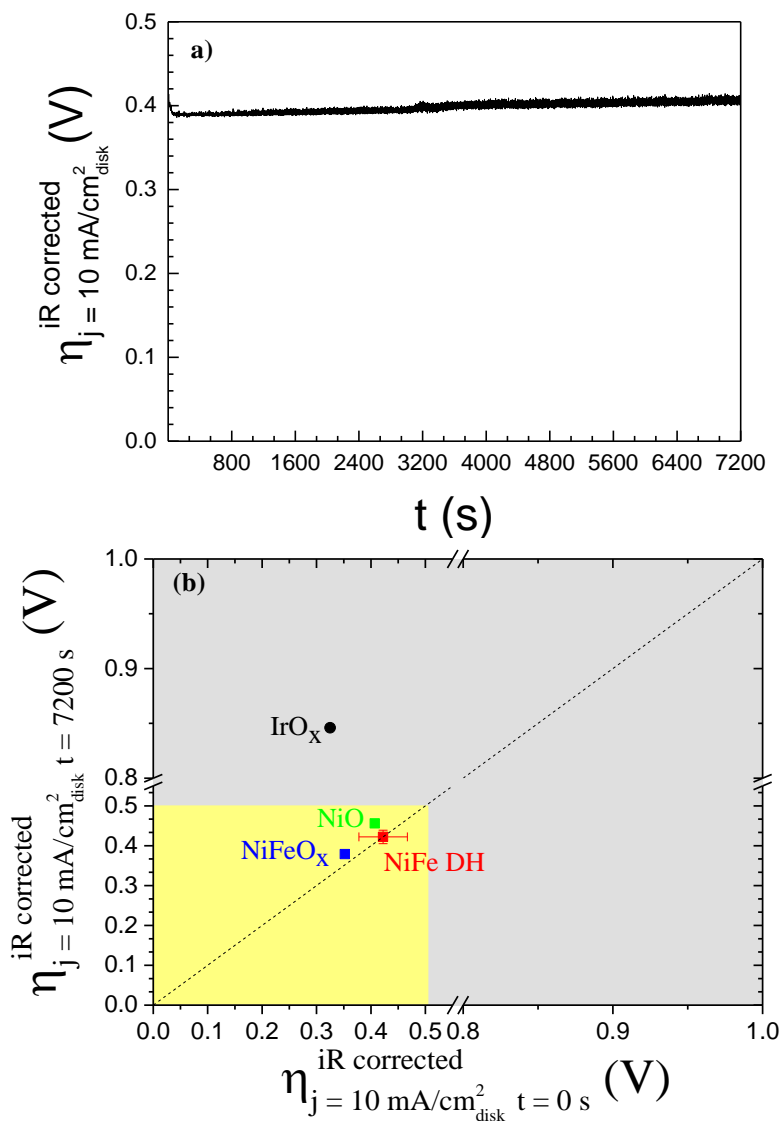


**Figure C7.** Stability of NiFe DH assessed by galvanostatic electrolysis. a) Evolution of the overpotential towards electrochemical water oxidation in KOH 0.1 M on NiFe DH, measured by applying a constant current density of  $10 \text{ mA cm}^2_{\text{disk}}$  during 2 h in hydrodynamic conditions (rotation rate: 1500 RPM). b) Overpotential at the end of the galvanostatic electrolysis towards electrochemical water oxidation on NiFe DH obtained from Figure C7a as a function of the initial overpotential. Additional points for IrO<sub>x</sub>, NiO and NiFeO<sub>x</sub> are provided for comparison, and correspond to a galvanostatic experiment performed in NaOH 1M, taken from McCrory *et al.*<sup>2</sup>



### Estimation of the Faradaic efficiency

The experiments were performed in rotating ring-disk electrode (RRDE) configuration. The Pt-ring electrode was set at 0.45 V vs. RHE so that the O<sub>2</sub> produced in the disk during the anodic scans was reduced, via 4 electrons to OH<sup>-</sup>, according the equation C1<sup>4</sup>:



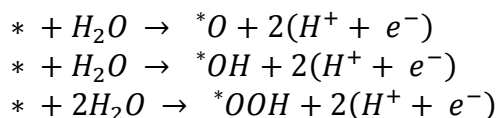
The faradaic efficiency ( $\varepsilon\%$ ) was calculated using the expression for the collection efficiency of the RRDE<sup>5</sup> given in Equation C2:

$$\varepsilon(\%) = \frac{i_{ring}}{N \cdot i_{disk}} \times 100 \quad (C2)$$

The collection efficiency (N) for the RRDE setup was calculated for the water oxidation reaction, using IrO<sub>2</sub> deposited on the Au-disk as electrocatalyst<sup>2</sup> and the number obtained was  $0.20 \pm 0.01$ , which is in close agreement with the collection factor obtained from the experiments with Fe(CN)<sub>6</sub><sup>3-</sup>/ Fe(CN)<sub>6</sub><sup>4-</sup> (N=0.23). The small difference between N calculated from water oxidation/oxygen reduction and the Fe(CN)<sub>6</sub><sup>3-</sup>/ Fe(CN)<sub>6</sub><sup>4-</sup> is attributed to the non-ideal outward flow of O<sub>2</sub>.<sup>1</sup>

### Estimation of the adsorption energies

The adsorption energies of \*O, \*OH and \*OOH, namely  $\Delta G_O$ ,  $\Delta G_{OH}$  and  $\Delta G_{OOH}$ , correspond to the reaction energies of the following reactions:



Where \* is a free adsorption site at the surface. The left leg of the volcanoes in Figures 2 and 3 are calculated as:  $\Delta G_{\text{LEFT}} = \Delta G_{\text{OOH}} - \Delta G_{\text{O}}$ . The right leg of the volcanoes in Figures 2 and 3 are calculated as:  $\Delta G_{\text{RIGHT}} = \Delta G_{\text{O}} - \Delta G_{\text{OH}}$ .

We note that in the case of the oxygen reduction reaction (ORR), namely the reaction opposite to the OER, solvation is essential to estimate accurate adsorption energies and the corrections for \*OH and \*OOH are on the order of  $\sim 0.5$  eV<sup>6</sup>. However, Norskov and coworkers have shown that solvation decreases as the electrode potential raises<sup>7</sup>. Among the reasons for the loss of solvation, we remark the formation of surface oxides, which disturb the formation of the long-ranged ice-like water layers over the surface within which adsorbates such as \*OH and \*OOH are fully solvated. This is why the modelling of the OER does not normally incorporate solvation corrections (see Man et al.<sup>8</sup>). Furthermore, earlier this year, Siahrostami and Vojvodic inspected the effects of solvation on the predicted OER overpotentials of various rutile oxides<sup>9</sup>. Note that they used exactly the same kind of volcano plots and exchange-correlation functional (RPBE) as in our study and concluded that “the OER activity trend is preserved in the presence of a water network”. They also find that oxides near the top of the volcano possess solvation energies the addition of which modifies the OER overpotentials by  $\sim 0.05$  V only. We conclude that solvation is typically not included in the OER modelling and that its addition does not alter the overall conclusions of Sabatier-type activity plots. Additionally, we would like to mention that we have considered a full coverage of adsorbed intermediates for the double hydroxides in this study (see Figure 1 in the main text and Figure C7 below). Thus, there exist hydrogen bonds between co-adsorbed oxygenates (\*OH with other vicinal \*OH and \*OOH species) which are accounted for in the adsorption energy trends without any need for external corrections.

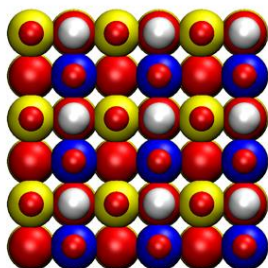
The volcano plots in Figures 3a and b in the main text correspond to a full-coverage regime in which different species populate the active sites as follows:

i) In Figure 3a, that is when the activity of Ni sites is evaluated, the M site was covered with \*O for M = Cr, Mn, Fe, Co, and the M site was covered with \*OH for M = Ni, Cu, Zn.

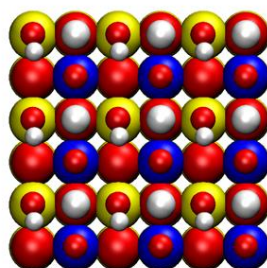
ii) In Figure 3b, that is when the activity of M sites is assessed, Ni sites are covered with \*OH.

These different configurations are provided in Figure C7.

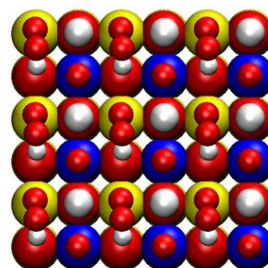
a) O @ Ni + O @ M



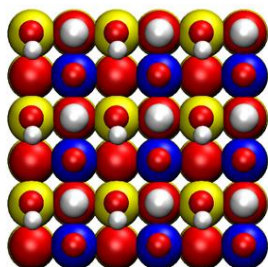
b) OH @ Ni + O @ M



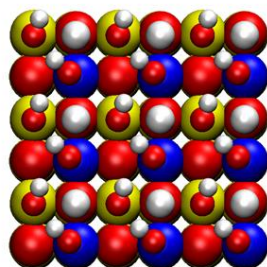
c) OOH @ Ni + O @ M



d) OH @ Ni + O @ M



e) OH @ Ni + OH @ M



f) OH @ Ni + OOH @ M

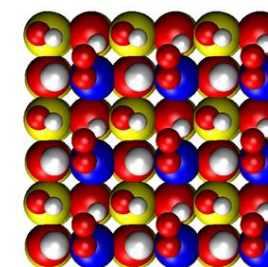


**Figure C7.** High coverage of OER adsorbates on model NiMOOH catalysts. When the activity of Ni sites is evaluated (Figure 3a), the adsorption energies of a) \*O, b) \*OH and c) \*OOH are calculated while the M site is covered with \*O for M = Cr, Mn, Fe, Co. When M = Ni, Cu, Zn, the M site is covered with \*OH, analogous to d)-f). When the activity of M sites is assessed (Figure 3b), the adsorption energies of c) \*O, d) \*OH, and e) \*OOH are calculated while Ni sites are covered with \*OH.

## REFERENCES

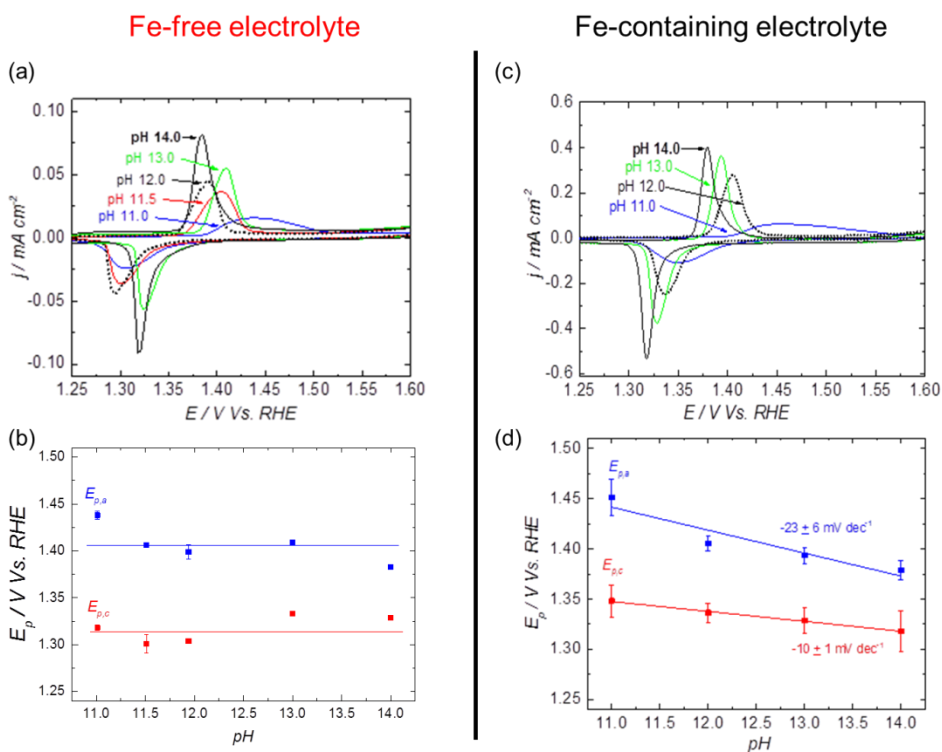
- (1) Lee, Y.; Suntivich, J.; May, K. J.; Perry, E. E.; Shao-Horn, Y. *J. Phys. Chem. Lett.* **2012**, *3*, 399.
- (2) McCrory, C. C.; Jung, S.; Peters, J. C.; Jaramillo, T. F. *J. Am. Chem. Soc.* **2013**, *135*, 16977.
- (3) Zhao, Y.; Hernandez-Pagan, E. A.; Vargas-Barbosa, N. M.; Dysart, J. L.; Mallouk, T. E. *J. Phys. Chem. Lett.* **2011**, *2*, 402.
- (4) Marković, N. M.; Schmidt, T. J.; Stamenković, V.; Ross, P. N. *Fuel Cells* **2001**, *1*, 105.
- (5) Bard Allen J., F. L. R. *Electrochemical Methods: Fundamentals and Applications*; 2nd ed., 2001.
- (6) Nørskov, J. K.; Rossmeisl, J.; Logadottir, A.; Lindqvist, L.; Kitchin, J. R.; Bligaard, T.; Jónsson, H. *J. Phys. Chem. B* **2004**, *108*, 17886.
- (7) Casalongue, H. S.; Kaya, S.; Viswanathan, V.; Miller, D. J.; Friebel, D.; Hansen, H. A.; Nørskov, J. K.; Nilsson, A.; Ogasawara, H. *Nat Commun* **2013**, *4*.
- (8) Man, I. C.; Su, H.-Y.; Calle-Vallejo, F.; Hansen, H. A.; Martínez, J. I.; Inoglu, N. G.; Kitchin, J.; Jaramillo, T. F.; Nørskov, J. K.; Rossmeisl, J. *ChemCatChem* **2011**, *3*, 1159.
- (9) Siahrostami, S.; Vojvodic, A. *J. Phys. Chem. C* **2015**, *119*, 1032.



## Appendix D: Supplementary Material for Chapter 5

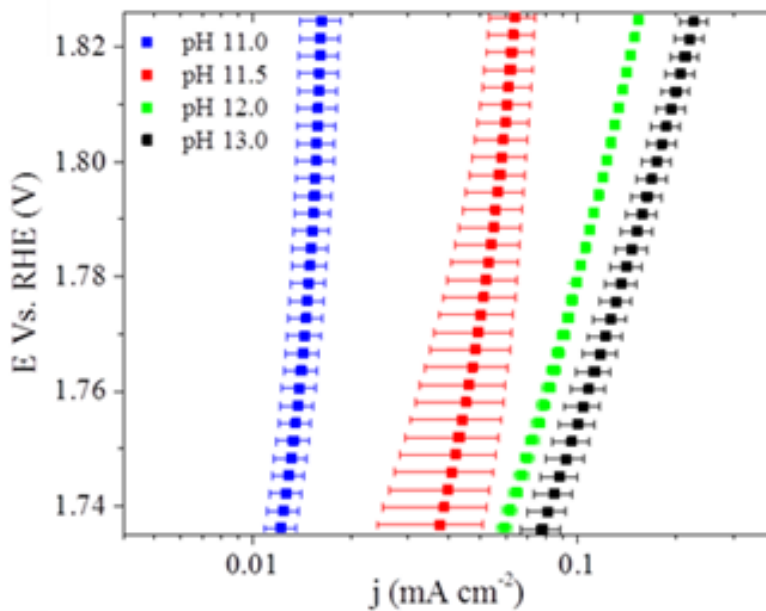
### *The Importance of Nickel Oxyhydroxide Deprotonation on its Activity towards Electrochemical Water Oxidation*

#### pH dependence of the potential for the $\text{Ni}^{2+}/\text{Ni}^{3+}$ redox transition: comparison between Fe-free and Fe-containing electrolytes



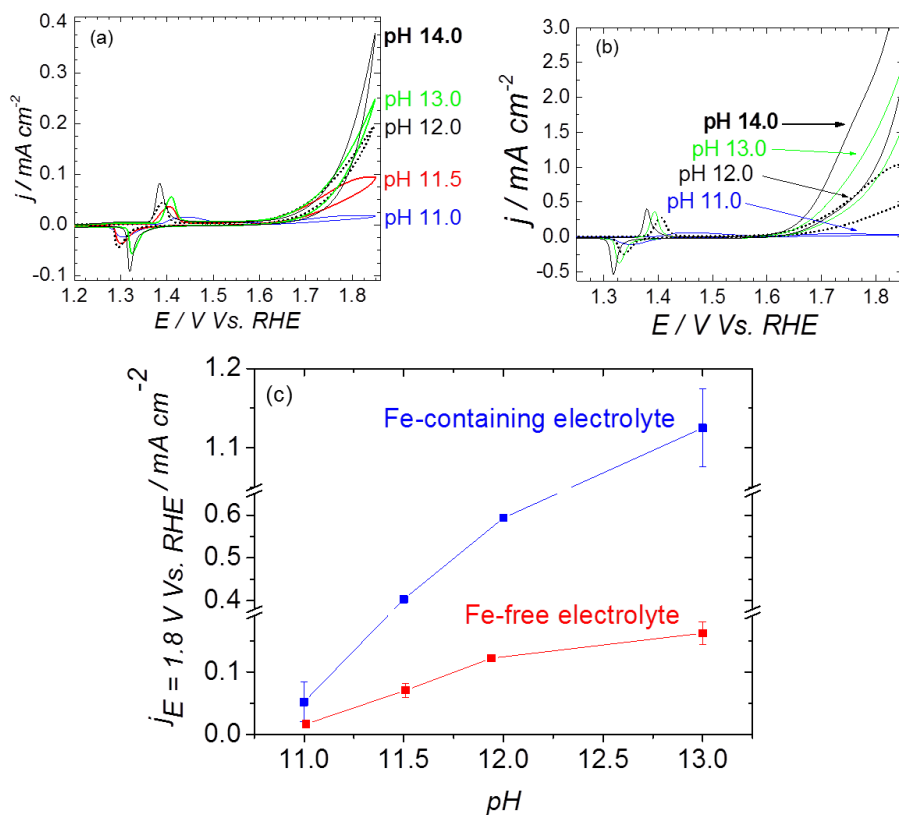
**Figure D1.** a) CVs of NiOOH acquired in purified (Fe-free) electrolyte, showing the changes in the  $\text{Ni}^{2+}/\text{Ni}^{3+}$  redox transition with the pH. Scan rate: 0.01 V/s. b) Position of the oxidation and reduction peaks for the  $\text{Ni}^{2+}/\text{Ni}^{3+}$  redox transition ( $E_{p,a}/E_{p,c}$ ) in a) as a function of pH. c) CVs acquired in unpurified Fe-containing electrolyte, showing the changes in the  $\text{Ni}^{2+}/\text{Ni}^{3+}$  redox transition with the pH. Scan rate: 0.01 V/s. d) Position of the oxidation and reduction peaks for the  $\text{Ni}^{2+}/\text{Ni}^{3+}$  redox transition ( $E_{p,a}/E_{p,c}$ ) in c) as a function of pH.

## Capacitance-corrected OER activity of NiOOH as a function of pH



**Figure D2.** OER activity obtained from the average of the current measured in the forward and backward scan in the polarization curves of NiOOH deposited on Au (capacitance-corrected). Measurements at pH's 11 – 13 were performed at constant ionic strength, adjusted to 0.1 M with  $\text{NaClO}_4$  except for pH 13, that solution was  $\text{NaOH}$  0.1 M.

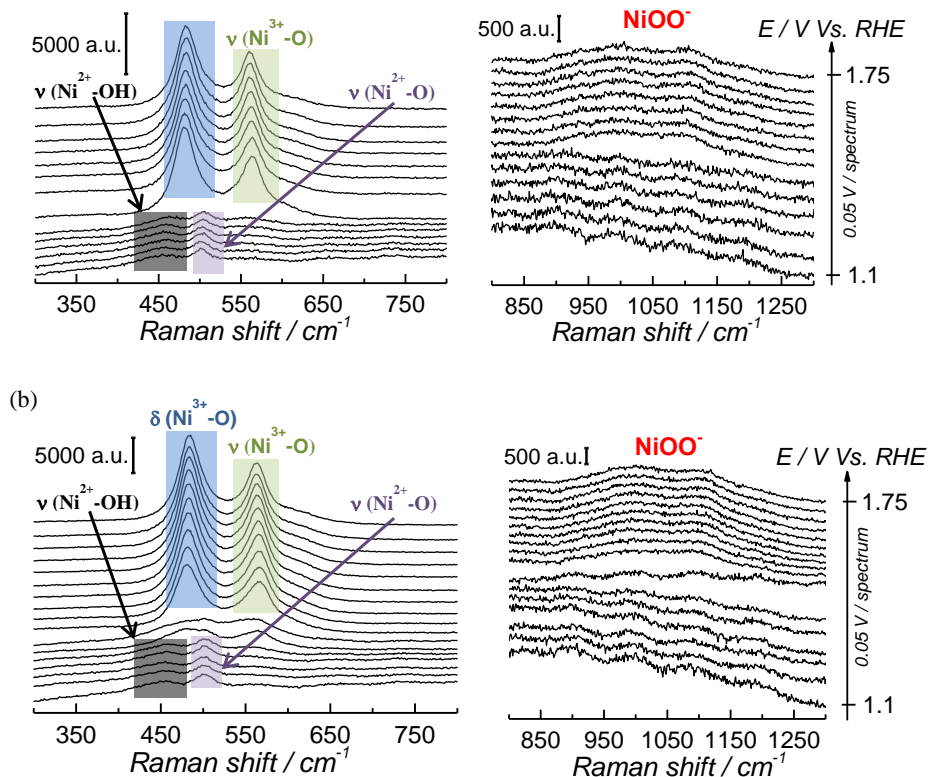
### The catalytic activity of NiOOH towards OER: the effect of iron impurities in the electrolyte



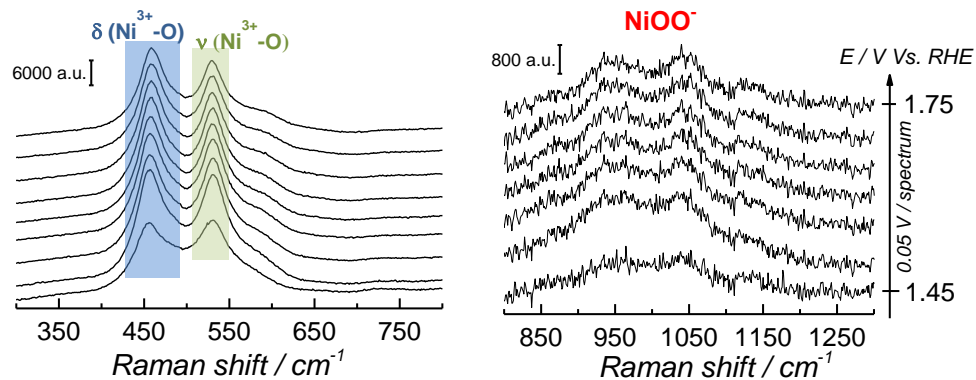
**Figure D3.** Effect of iron impurities on the activity of NiOOH towards OER. Measurements at pH's 11 – 13 were performed at constant ionic strength, adjusted to 0.1 M with NaClO<sub>4</sub>. Solutions at pH 13 and pH 14 were NaOH 0.1 M and 1 M respectively. Scan rate: 0.01 V/s. a) CVs measured in Fe-free electrolyte. b) CVs measured in Fe-containing electrolyte. c) Capacitance-corrected activity of NiOOH towards OER as a function of pH, the activity was measured from the CVs a) and b) as the average of the backwards and forward current density at 1.8 V vs. RHE.



## Additional SERS spectra of NiOOH in the Fe-free electrolyte



**Figure D4.** SER spectra obtained at constant potential during the electrochemical oxidation of  $\text{Ni}(\text{OH})_2$  and the subsequent OER on NiOOH at different pH's. The ionic strength of the solution was fixed to 0.1 M with  $\text{NaClO}_4$ . The left panel presents the spectra in the wavenumber region 300 – 800  $\text{cm}^{-1}$  and the right panel presents the wavenumber region 800 – 1300  $\text{cm}^{-1}$ : a) pH 11.5, b) pH 14.0.

SERS experiments in solutions prepared with  $\text{H}_2^{18}\text{O}$ 

**Figure D5.** SER spectra obtained at constant potential during the electrochemical oxidation of  $\text{Ni}(\text{OH})_2$  and the subsequent OER on  $\text{NiOOH}$  at pH 13. The electrolyte was prepared in  $\text{H}_2^{18}\text{O}$ . The left panel presents the spectra in the wavenumber region 300 – 800  $\text{cm}^{-1}$  and the right panel presents the wavenumber region 800 – 1300  $\text{cm}^{-1}$ .

**Position of the Raman peaks of NiOOH in electrolytes prepared with H<sub>2</sub><sup>16</sup>O and H<sub>2</sub><sup>18</sup>O**

**Table D1.** Position of the Raman peaks associated with the vibrations  $\delta(\text{Ni}^{3+}\text{-O})$ ,  $\nu(\text{Ni}^{3+}\text{-O})$  and  $\text{NiOO}^-$  as a function of the oxygen isotope in the electrolyte. The spectra were obtained in NaOH 0.1 M in potentiostatic conditions.

E (V vs. RHE)	$\delta(\text{Ni}^{3+}\text{-O})$		$\nu(\text{Ni}^{3+}\text{-O})$		$\text{NiOO}^-$			
	<sup>16</sup> O	<sup>18</sup> O	<sup>16</sup> O	<sup>18</sup> O	<sup>16</sup> O	<sup>18</sup> O	<sup>16</sup> O	<sup>18</sup> O
1.65	481 ± 1	459 ± 3	561 ± 1	530 ± 5	986 ± 9	908 ± 9	1093 ± 2	1054 ± 5
1.7	482 ± 1	460 ± 1	561 ± 1	531 ± 3	991 ± 8	891 ± 12	1097 ± 8	1054 ± 8
1.75	481 ± 1	458 ± 3	560 ± 1	529 ± 5	991 ± 13	896 ± 8	1096 ± 7	1068 ± 6

## Appendix E: Supplementary Material for Chapter 6

*Iridium-based Double Perovskites for Efficient and Cost Effective Water Oxidation in Acid Media*

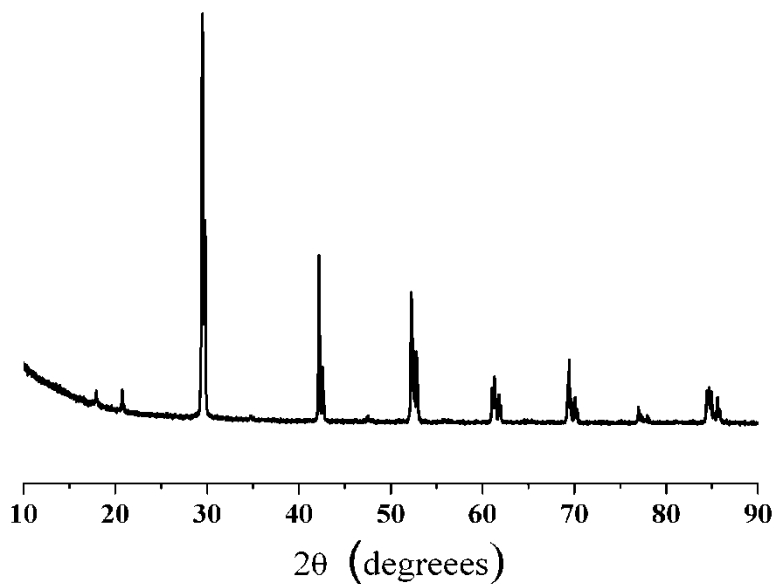


**Figure E1.** Powder XRD for the Ba<sub>2</sub>LaIrO<sub>6</sub> double perovskite

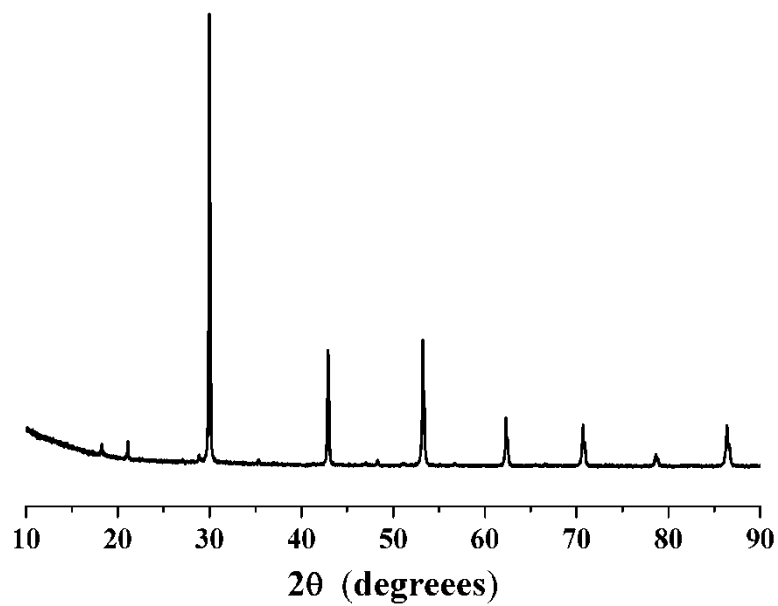


**Figure E2.** Powder XRD for the  $\text{Ba}_2\text{CeIrO}_6$  double perovskite

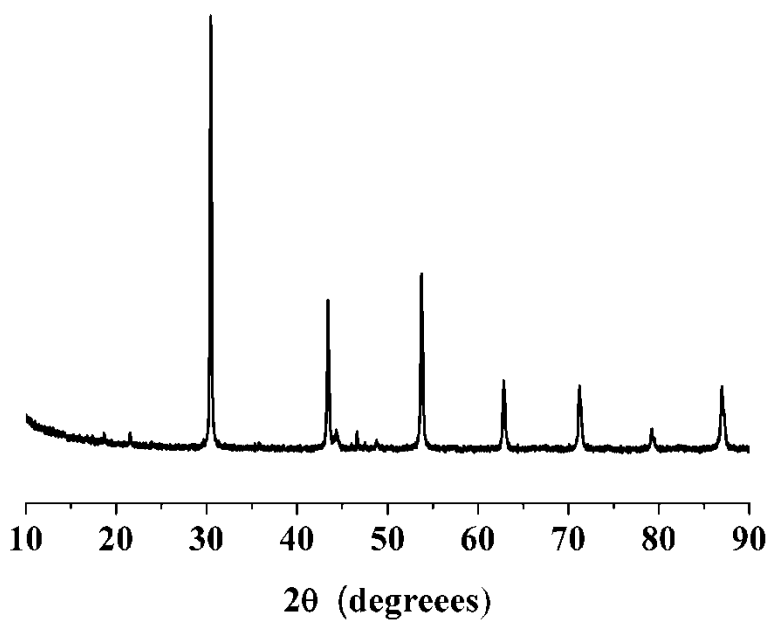


**Figure E3.** Powder XRD for the  $\text{Ba}_2\text{PrIrO}_6$  double perovskite

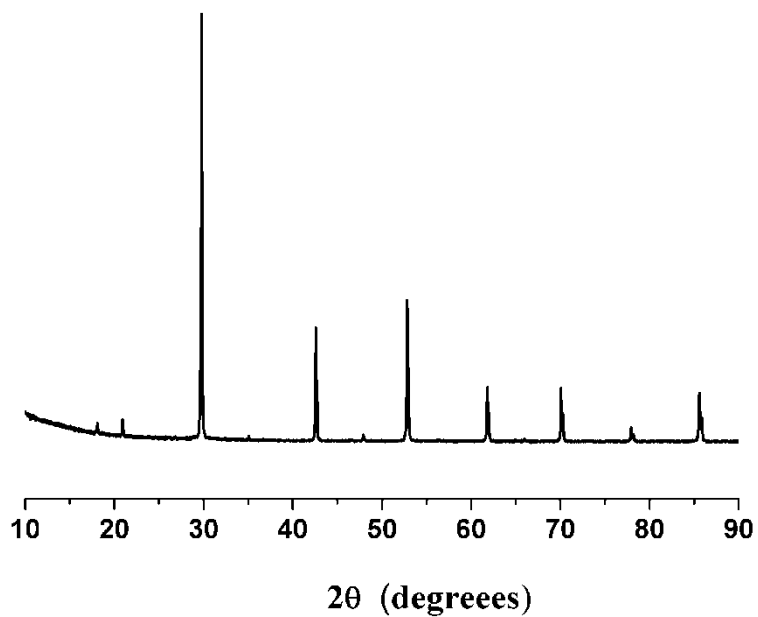


**Figure E4.** Powder XRD for the Ba<sub>2</sub>NdIrO<sub>6</sub> double perovskite

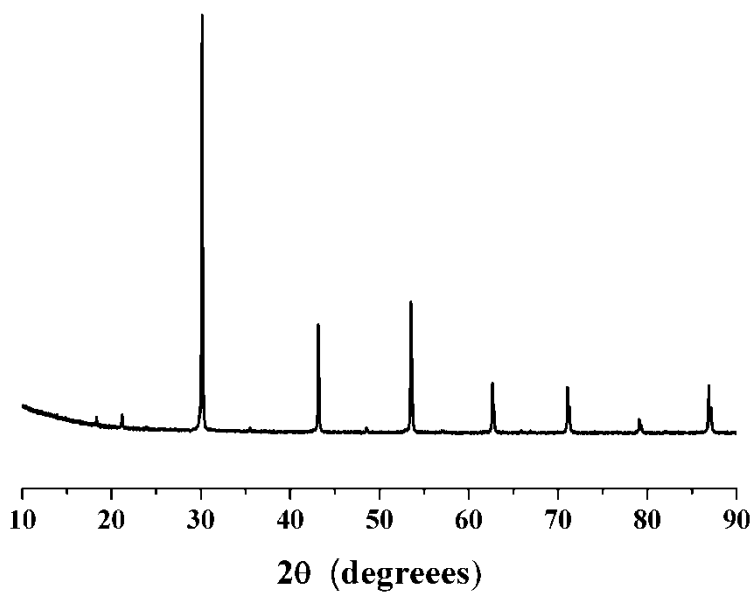


**Figure E5.** Powder XRD for the Ba<sub>2</sub>TbIrO<sub>6</sub> double perovskite



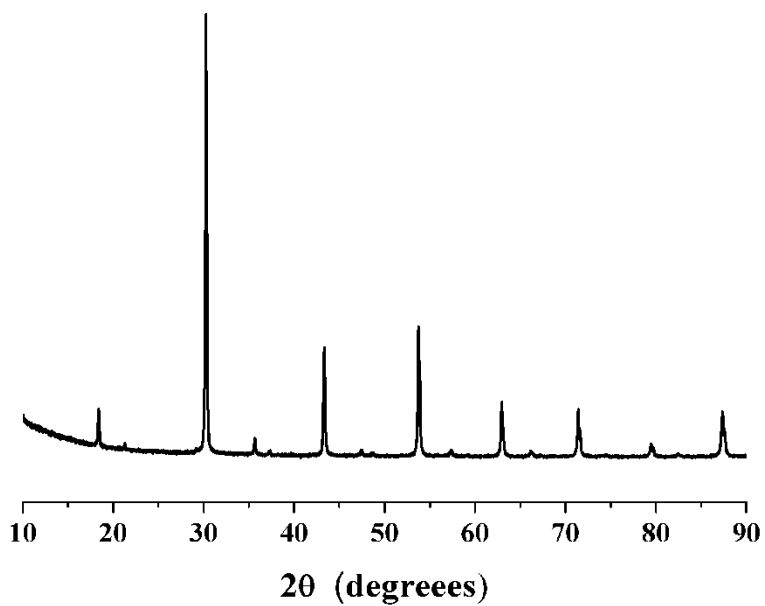


**Figure E6.** Powder XRD for the Ba<sub>2</sub>YIrO<sub>6</sub> double perovskite

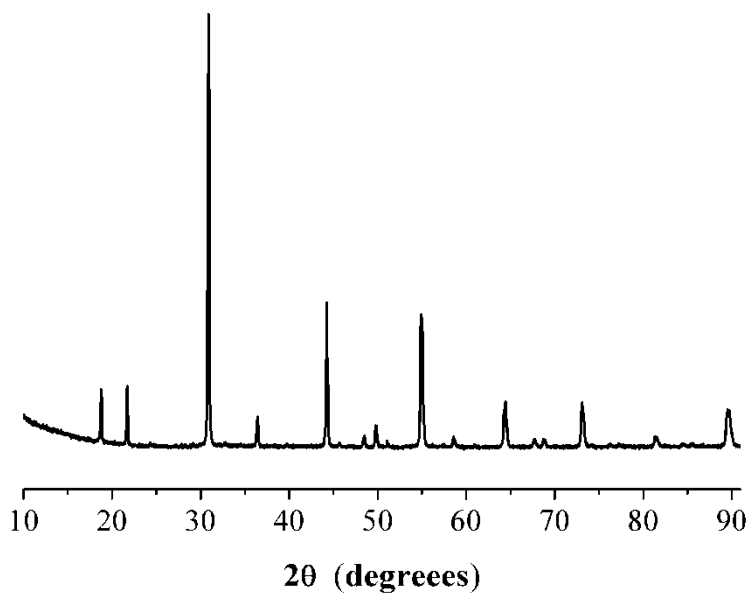


**Figure E7.** Powder XRD for the  $\text{Sr}_2\text{YIrO}_6$  double perovskite

**Table E1.** Tafel slope for the water splitting reaction in 0.1 M HClO<sub>4</sub> for IrO<sub>2</sub> and the iridium-based double perovskites. Currents were measured in steady-state conditions. Rotation rate: 1500 RPM.

	<b>Tafel slope (mV/dec)</b> <b>(E = 1.5-1.6 V vs. RHE)</b>	<b>Tafel slope (mV/dec)</b> <b>(E &gt; 1.6 V vs. RHE)</b>
<b>IrO<sub>2</sub></b>	57 ± 1	115 ± 13
<b>Ba<sub>2</sub>LaIrO<sub>6</sub></b>	59 ± 3	127 ± 10
<b>Ba<sub>2</sub>CeIrO<sub>6</sub></b>	57 ± 7	121 ± 12
<b>Ba<sub>2</sub>PrIrO<sub>6</sub></b>	54 ± 3	106 ± 17
<b>Ba<sub>2</sub>NdIrO<sub>6</sub></b>	59 ± 4	136 ± 1
<b>Ba<sub>2</sub>TbIrO<sub>6</sub></b>	61 ± 3	118 ± 9
<b>Ba<sub>2</sub>YIrO<sub>6</sub></b>	67 ± 4	196 ± 23

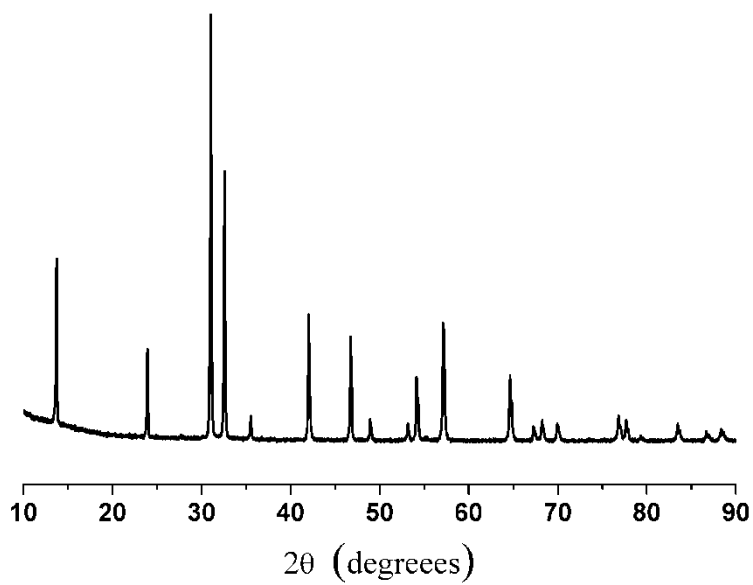


**Figure E8.** Powder XRD for  $\text{Sr}_2\text{IrO}_4$  layered perovskite Ruddlesden-Popper phase

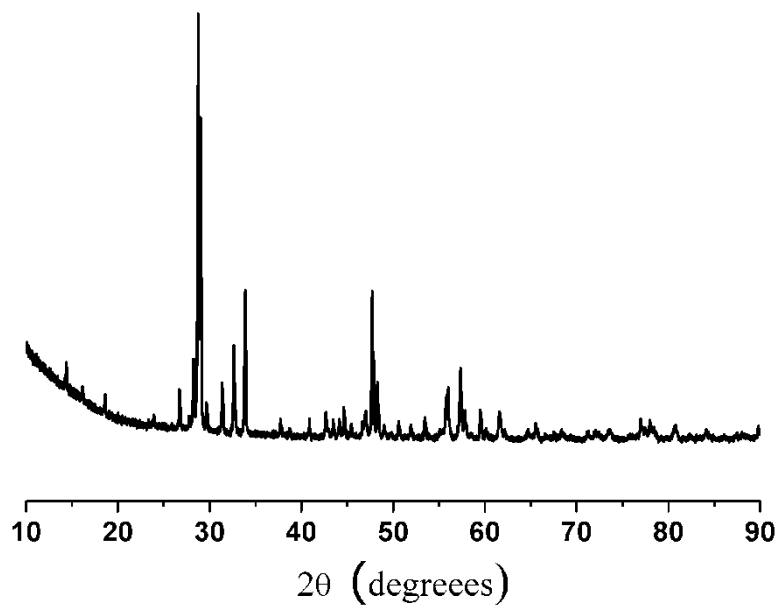


**Figure E9.** Powder XRD for  $\text{Pr}_3\text{IrO}_7$  fluorite-like phase

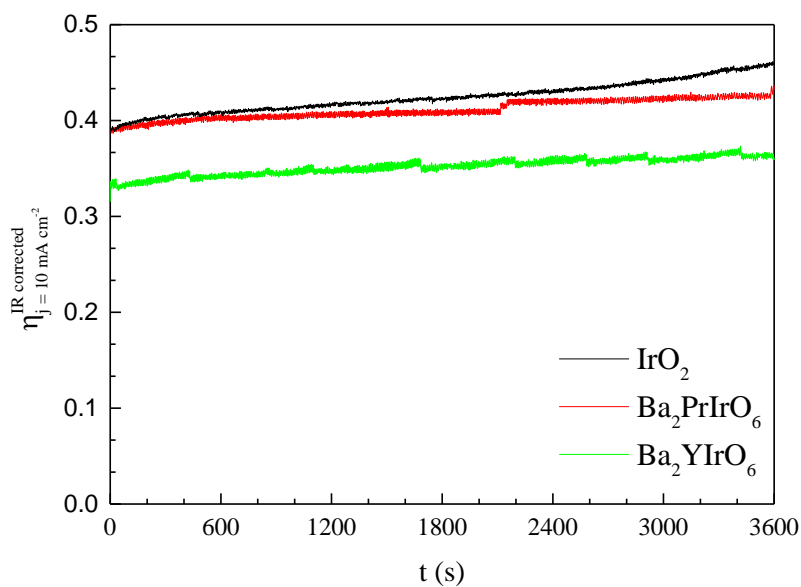


**Figure E10.** Evolution of the overpotential towards electrochemical water oxidation in 0.1 M  $\text{HClO}_4$   $\text{Ba}_2\text{PrIrO}_6$  /  $\text{Ba}_2\text{YIrO}_6$  double perovskites, measured by applying a constant current density of  $10 \text{ mA cm}_{\text{disk}}^{-2}$  during 1 h in hydrodynamic conditions (rotation rate: 1500 RPM). The stability of  $\text{IrO}_2$  nanoparticles is presented for comparison.

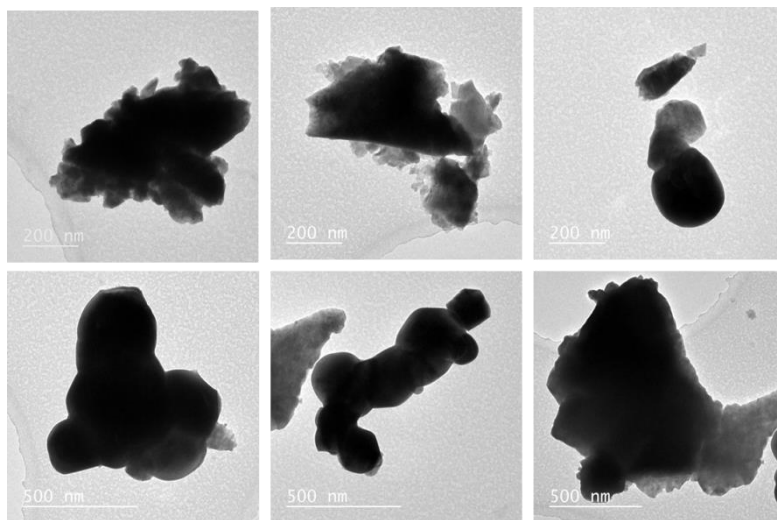


**Figure E11.** TEM images of the pristine sample of Ba<sub>2</sub>LaIrO<sub>6</sub> double perovskite.

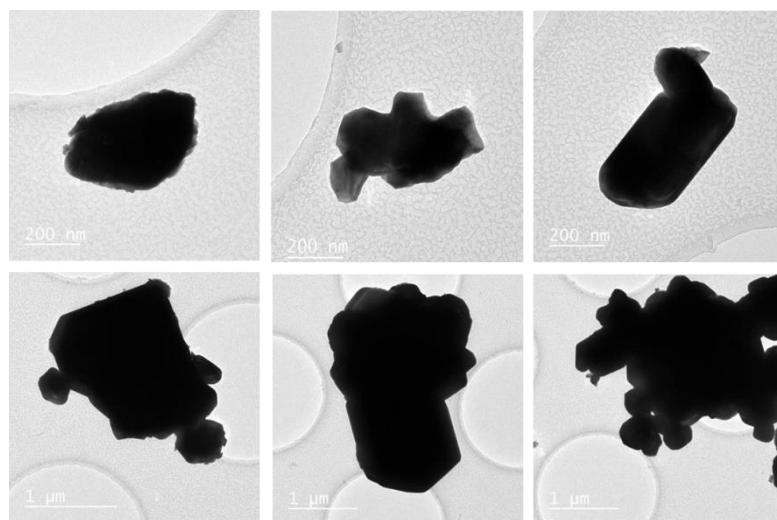


**Figure E12.** TEM images of the pristine sample of Ba<sub>2</sub>CeIrO<sub>6</sub> double perovskite.

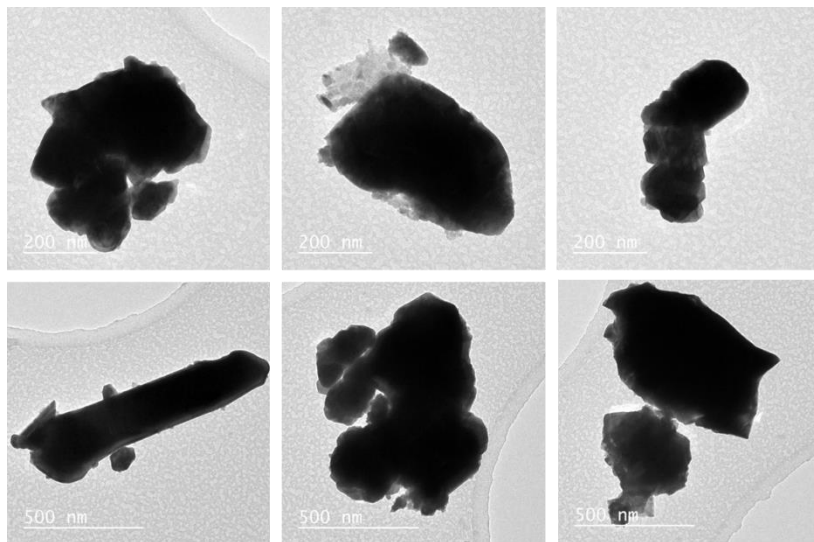


**Figure E13.** TEM images of the pristine sample of Ba<sub>2</sub>PrIrO<sub>6</sub> double perovskite.

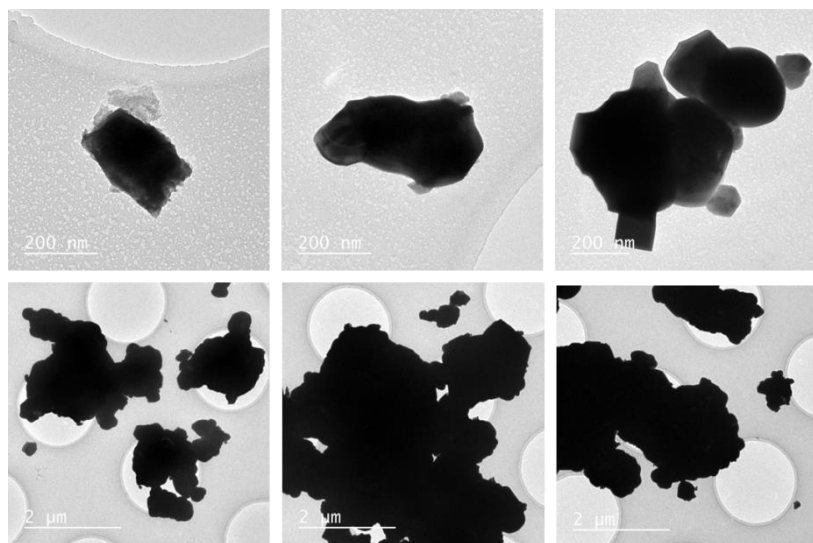


**Figure E14.** TEM images of the pristine sample of Ba<sub>2</sub>NdIrO<sub>6</sub> double perovskite.



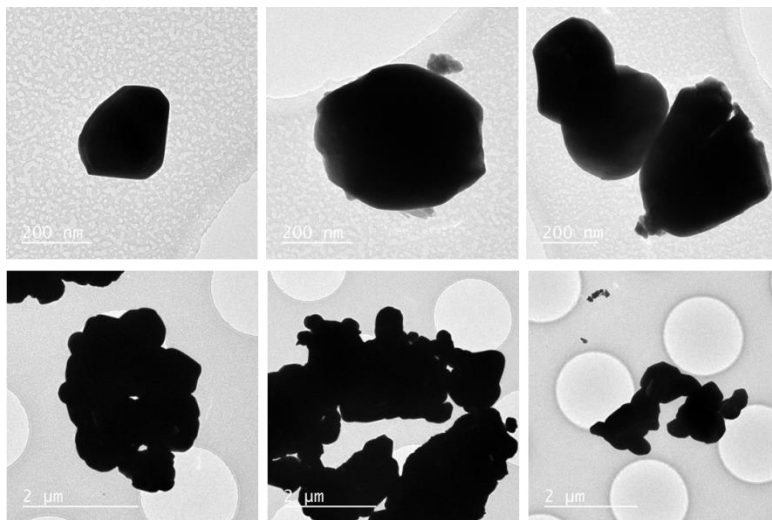


**Figure E15.** TEM images of the pristine sample of Ba<sub>2</sub>TbIrO<sub>6</sub> double perovskite.

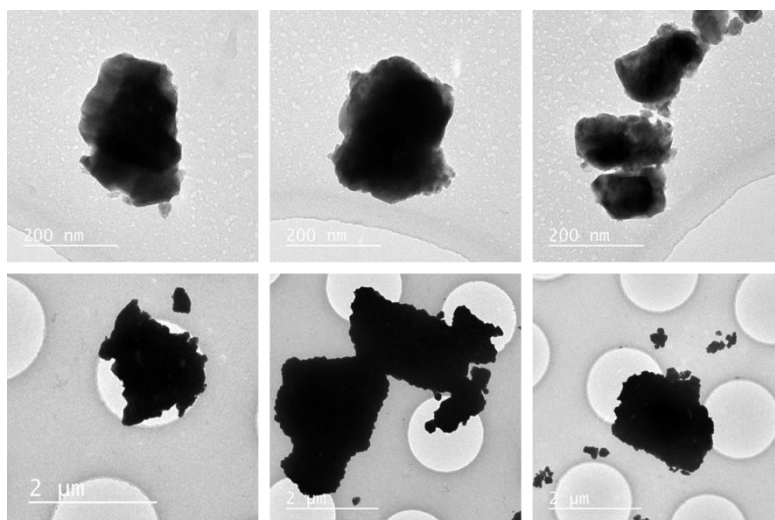


**Figure E16.** TEM images of the pristine sample of Ba<sub>2</sub>TbIrO<sub>6</sub> double perovskite.

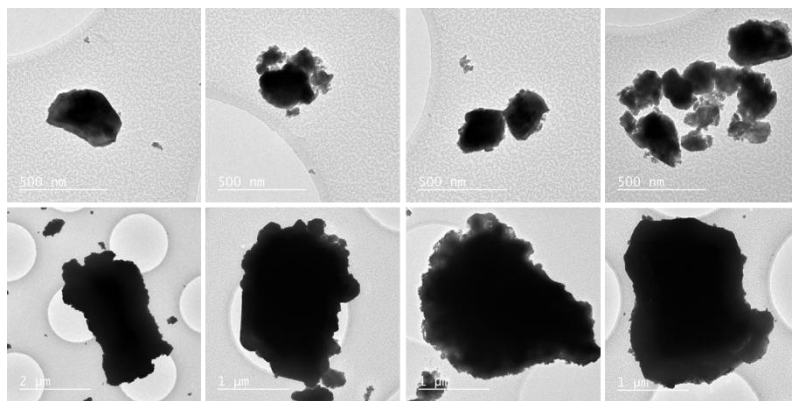


**Figure E17.** TEM images of  $\text{Ba}_2\text{PrIrO}_6$  double perovskite after leaching in  $\text{HClO}_4$  0.1 M for 48 h.

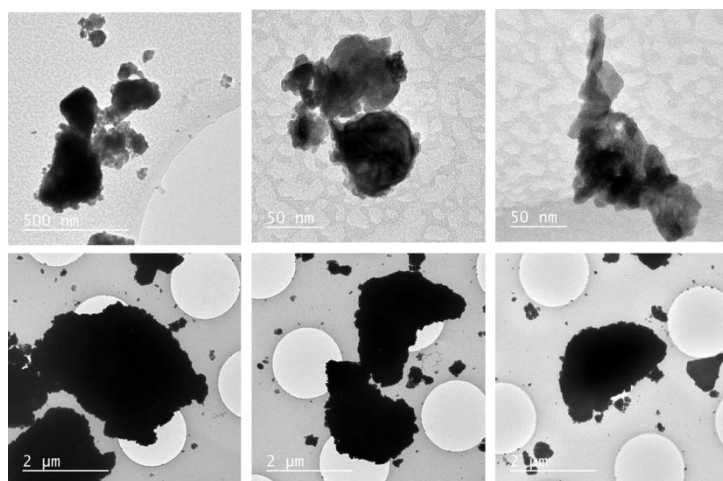


**Figure E18.** TEM images of  $\text{Ba}_2\text{PrIrO}_6$  double perovskite after leaching in 0.1 M  $\text{HClO}_4$  + 4 M  $\text{H}_2\text{O}_2$  for 48 h.

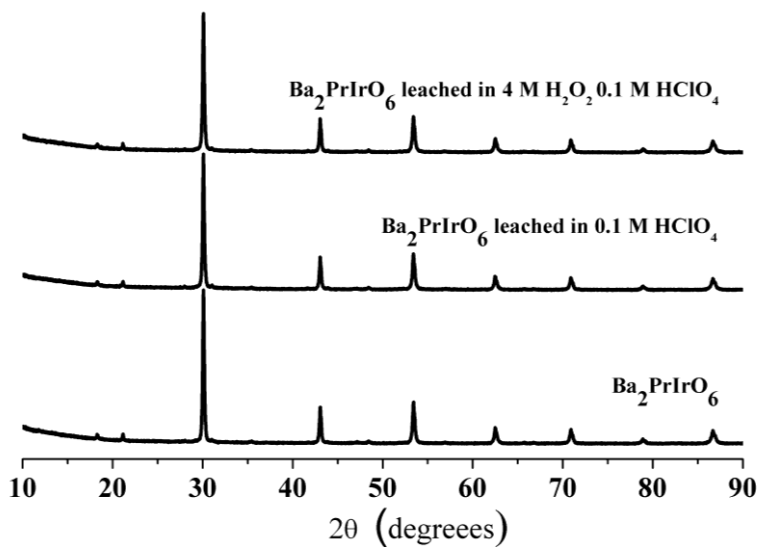


**Figure E19.** Powder XRD of the  $\text{Ba}_2\text{PrIrO}_6$  before and after the leaching treatments. XRD pattern of the  $\text{Ba}_2\text{PrIrO}_6$  pristine sample is presented for comparison.

**XPS analysis of the pristine and leached Ba<sub>2</sub>PrIrO<sub>6</sub> double perovskite**

The results of the XPS analysis of the Ba<sub>2</sub>PrIrO<sub>6</sub> double perovskite before and after exposure to the oxidizing environment are presented in Figure E20.

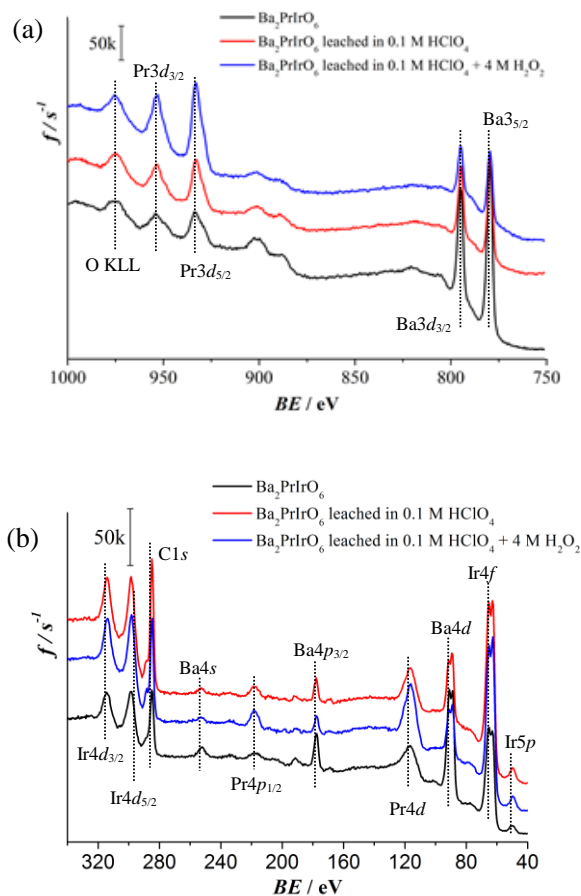


**Figure E20.** XPS spectra of pristine Ba<sub>2</sub>PrIrO<sub>6</sub> before and after the leaching treatments. a) Binding energy region 750 – 1000 eV. b) Binding energy region 40 – 340 eV.

It is clearly shown in Figure E20 that the pristine double perovskite contains a much larger contribution of Ba ( $3d_{3/2}$ , 794.9 eV;  $3d_{5/2}$ , 779.6 eV) relative to Pr ( $3d_{3/2}$ , 953.4 eV;  $3d_{5/2}$ , 933.0 eV) compared to the leached samples. The surface of the double perovskite enriches with praseodymium upon leaching with hydrogen peroxide and perchloric acid, which is indicated by the relative intensities in Figure E20. The intensity of the peaks attributed to iridium ( $Ir4d_{3/2}$ , 313.9;  $Ir4d_{5/2}$ , 298.1 eV and  $Ir4f$ , 63.8 eV) increases for the sample leached in 0.1 M HClO<sub>4</sub>, however, the oxidative treatment in 0.1 M HClO<sub>4</sub> + 4 M H<sub>2</sub>O<sub>2</sub> slightly reduces the intensity of the iridium peaks, indicating that the noble metal started to leach.

The surface composition of the pristine and leached Ba<sub>2</sub>PrIrO<sub>6</sub> samples is summarized in table E2. The XPS results show that the relative atomic composition in the pristine double perovskite is very close to the expected values, indicating that the surface exhibits the same composition as the bulk of the double perovskite. Again, the results show the surface composition of the Ba<sub>2</sub>PrIrO<sub>6</sub> enriches in iridium and praseodymium upon the leaching treatments, whereas the barium is depleted from the surface.

**Table E2:** Surface composition of Ba, Pr and Ir in the pristine Ba<sub>2</sub>PrIrO<sub>6</sub> and after the leaching treatments with 0.1 M HClO<sub>4</sub> and 0.1 M HClO<sub>4</sub> + 4 M H<sub>2</sub>O<sub>2</sub>, obtained from XPS analysis. The expected values were obtained from the chemical formula of the compound reported by Fu and Ijdo<sup>1</sup>.

	Ba	Pr	Ir
<b>Expected values</b>	2.00	1.00	1.00
<b>Pristine Ba<sub>2</sub>PrIrO<sub>6</sub></b>	2.46	0.97	1.00
<b>Ba<sub>2</sub>PrIrO<sub>6</sub> leached in 0.1 M HClO<sub>4</sub></b>	0.85	0.77	1.00
<b>Ba<sub>2</sub>PrIrO<sub>6</sub> leached in 0.1 M HClO<sub>4</sub> + 4 M H<sub>2</sub>O<sub>2</sub></b>	0.60	1.39	1.00

The change in the oxidation state of barium, praseodymium and iridium in the samples was analyzed using the high-resolution scans of the core-level in the XPS spectra. The oxidizing treatment did not eliminate or change the adventitious carbon signal, allowing the use of the

C1s signal as energy calibration at 284.8 eV (see Figure E20b). The deconvolution analysis of the XPS spectra shows that the surface of the double perovskite contains additional oxidation states different from the bulk composition (see Figure E21).

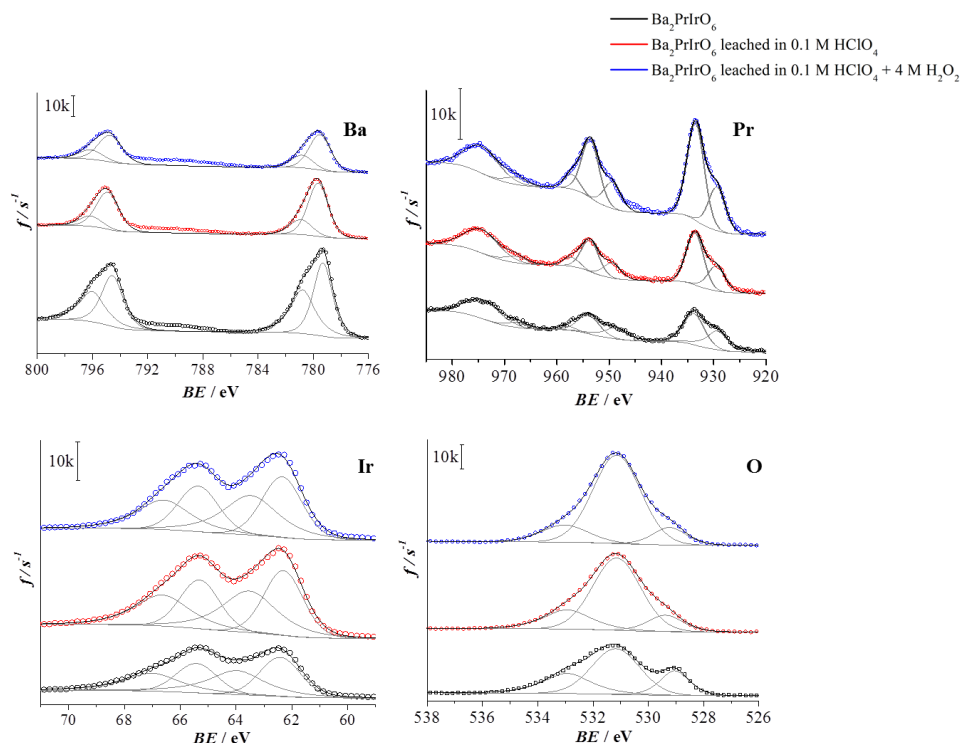


**Figure E21:** Core-level XPS spectra ( $Ba3d$ ,  $Pr3d$ ,  $Ir4f$  and  $O1s$ ) of  $Ba_2PrIrO_6$  before and after the leaching treatments.

The  $Ba3d$  core-level spectra in Figure E21 show the  $3d_{3/2}$  and  $3d_{5/2}$  contributions with spin-orbit coupling of 15.3 eV. The deconvolution was carried out with fixed 3:2 intensity ratios to exclude possible Pr MNN overlap at 797 eV and Ba shake-off features on the lower binding energies side of the  $Ba3d_{3/2}$  signal. The deconvoluted spectra of the  $Ba3d_{3/2}$  peak show two  $Ba^{2+}$  phases, one that can be related to the bulk perovskite (*ca.* 779.5 eV) and a different surface phase at *ca.* 780.8 eV)<sup>2-4</sup>. The spectra of pristine  $Ba_2PrIrO_6$  look similar to

other Ba-containing perovskites (*e.g.* BaTiO<sub>3</sub>) with a typical high-energy shoulder at *ca.* 1.3 eV above the main peak with an intensity ratio of around 0.6<sup>4,5</sup>. The leaching of barium from the Ba<sub>2</sub>PrIrO<sub>6</sub> double perovskite surface is accompanied with a relative decrease in the high-energy component, indicating removal of the surface phase and exposure of the barium-bulk phase. Furthermore, the typical Ba perovskite binding energy shifts approximately 0.3 eV to higher binding energies, indicating the change in environment to a more oxidized character<sup>6</sup>. The oxidizing treatment has a detrimental effect on the Ba content, heavily perturbing both the Ba surface and bulk phase. The ionic character of Ba in addition to its location in the cavity of the PrO<sub>6</sub>/IrO<sub>6</sub> octahedra may be the cause of its easier exclusion from the structure.

The Pr3*d* core-level spectra (see Figure E21) consist of two main signals from the ground state 4*f* configuration with spin-orbit coupling of 20.1 eV and accompanying shoulders and shake-off features resulting from a mixture of final state configurations<sup>7,8</sup>. The signals were recorded including the O1s Auger line to properly assess the distinct features that indicate a mixture of tri- and tetravalent species. The Pr3*d*<sub>5/2</sub> and Pr3*d*<sub>3/2</sub> signals of the pristine double perovskite are broad, with a FWHM of 4.7 eV, but the main peaks can be unambiguously fitted with the statistical 3:2 intensity ratio and 20.1 eV spin-orbit coupling, indicating that mainly Pr<sup>3+</sup> is present<sup>9</sup>. The 3*d*<sub>5/2</sub> binding energy of 933.8 eV agrees well with the binding energy of praseodymium in a PrAlO<sub>3</sub> perovskite lattice<sup>10</sup>, approximately 1.0 eV above the value reported for Pr<sub>2</sub>O<sub>3</sub><sup>7,11</sup>. The satellite energy separation of both signals is large, in the range of the reported values for trivalent Pr in highly electronegative ligand orientation<sup>12</sup>. Satellite spin-orbit coupling of 19.4 eV is lower than the expected (*ca.* 20.5 eV), and shake-off in the 3*d*<sub>3/2</sub> region is visible around 958 eV indicating Pr<sup>4+</sup> contributions, with PrO<sub>2</sub> nature<sup>11,13</sup>. The main and satellite relative intensity ratios of 0.6 are in the upper limit of trivalent species, and in addition to the abovementioned features, this indicates mixed-valence praseodymium species present in the perovskite structure. The acid treatment induced subtle changes in the spectra of praseodymium, suggesting minor but notable changes in the perovskite surface environment. The binding energy of the main peak shifted 0.3 eV to lower energy, and the width narrowed to FWHM values of 3.9 eV. Moreover, the satellite energy separation decreased and coincides with values for Pr<sub>2</sub>O<sub>3</sub>. Similarly, the

satellite intensity ratio of the  $3d_{5/2}$  signal is reduced to values very close to the value in  $\text{Pr}_2\text{O}_3$ <sup>12</sup>. The leaching treatment induces the removal of praseodymium from the perovskite through surface oxidation to form other phases with  $\text{Pr}^{3+}$ . The Ba:Pr ratio is approximately 1:2, which might indicate the formation of a  $\text{Pr}_2\text{BaO}_4$  spinel surface phase<sup>13</sup>.

The Ir4*f* core-level spectra show two broad signals separated by an extraordinary high saddle between  $4f_{5/2}$  and  $4f_{7/2}$ , indicating two superimposed spectra (see Figure E21)<sup>14</sup>. The deconvolution yields two contributions with spin-orbit coupling of 3.0 eV and different FWHM. The high binding energy peak is probably broader as a result of conduction band interaction during the photoemission process<sup>15,16</sup>. The binding energy values for the  $4f_{7/2}$  peak of 62.4 and 64.0 eV are about 0.3 eV higher than reported for iridium compounds with  $\text{Ir}^{4+}$ , the difference may be attributed to electronic charge transfer with praseodymium in the perovskite<sup>17,18</sup>. It is striking that the high binding energy peak shifts 0.5 eV towards lower binding energies after the oxidizing treatments, while the low binding energy peak value of 62.4 eV is unchanged. Moreover, the 1:1 relative ratio of the two contributions is maintained after the oxidizing treatment. Taking into account the formal  $\text{Ir}^{4+}$  valence of the bulk perovskite, the prominent saddle and increasing suspicion of  $\text{Pr}^{3+}$  contributions, the system is likely bivalent with  $\text{Ir}^{4+}$  and  $\text{Ir}^{5+}$  present in roughly equivalent ratio<sup>1</sup>.

The O1*s* core-level spectra have been resolved with three peaks to distinguish between the contributions of the metal oxides and the surface-adsorbed species (see Figure E21). The main peak of the pristine double perovskite is located around 531 eV and is accompanied by a high binding energy shoulder and a low binding energy peak at 529 eV. The main peak is either ascribed directly to the constitutional metal oxide, or more indirectly to oxyhydroxide or metal carbonate signals originating from interactions with the metal oxide surface<sup>4,11,15,17-20</sup>. The value of 531.1 eV agrees as well with ionic Ba-O-V bonds of non-bridging oxygen in barium vanadophosphate glasses, corresponding to a Ba-O coordination resembling the one in perovskite<sup>21</sup>. The low binding energy peak is ascribed to the O1*s* signal of a lattice oxygen, more specific from the lattice oxygen bound to  $\text{Pr}^{3+}$  or  $\text{Pr}^{4+}$ <sup>11,18,19</sup>. The O1*s* metal oxide contribution of perovskite-type  $\text{BaTiO}_3$  has a similar value of 529.0 eV, which is identical to other Pr-based perovskites such as  $\text{PrCoO}_3$ , and mixed  $\text{PrCaMnO}_3$ ,



once more indicating overlap of different metal-oxide signals<sup>4</sup>. This lattice oxygen binding energy is somewhat on the low side for Ir<sup>4+</sup> compounds, however, these values are not reported for perovskite phases<sup>17</sup>. In all abovementioned analyses, the 533 eV peak is assigned to surface contamination from adsorbed water or related hydroxide species. The effect of the oxidizing treatment on the O1s spectra is clear; the main peak further exceeds the high binding energy shoulder and lower binding energy peak. The lattice oxygen contribution is decreased to a minor shoulder, and its binding energy shifts to higher values. Thus, the oxyhydroxide and metal carbonate contribution has increased with respect to the surface contaminants and lattice oxygen, indicating that the surface coverage of the perovskite metal-oxide phase increases. The shift in binding energy is observed as well for BaTiO<sub>3</sub> perovskites, where the lattice oxygen signal at 529.0 eV shifted to 529.3 eV after prolonged oxidation times, displaying the electronic interaction of the bulk with the oxidized surface<sup>4</sup>. A shift in binding energy of the lattice oxygen in the case of Pr would imply a reduction from Pr<sup>4+</sup> to Pr<sup>3+</sup>, which could indicate a surface reorganization with other metals into different mixed-valence phases<sup>13</sup>.

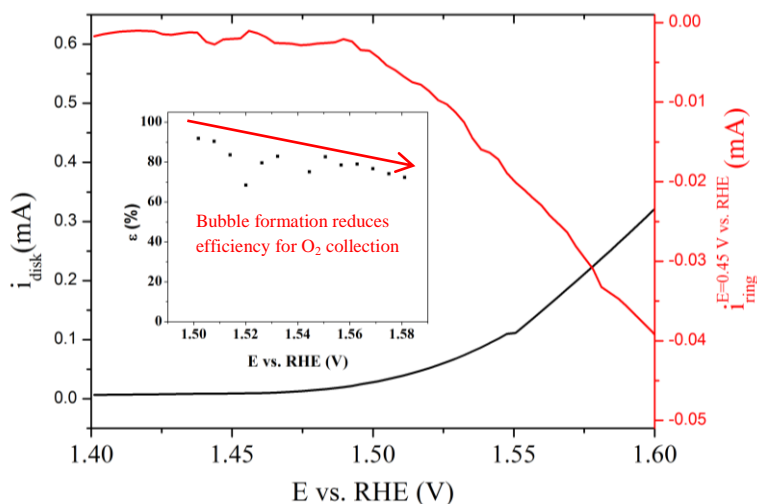
Summarizing, the deconvolution analysis of the XPS Ba, Pr, Ir and O core-levels indicate that next to the tetravalent Pr<sup>4+</sup>/Ir<sup>4+</sup> valence pair, a surface phase exists containing Pr<sup>3+</sup> and Ir<sup>5+</sup> (see Figure E21), however, the chemical nature of these species cannot be confirmed. The oxidizing treatment greatly perturbs the surface of the perovskite, majorly reducing the Ba content to values below that of Pr and Ir. The leaching further enhances the differences in the oxidation state, increasing the Ir<sup>5+</sup> contribution.

### Faradaic efficiency of Ba<sub>2</sub>PrIrO<sub>6</sub> towards OER in 0.1 M HClO<sub>4</sub>

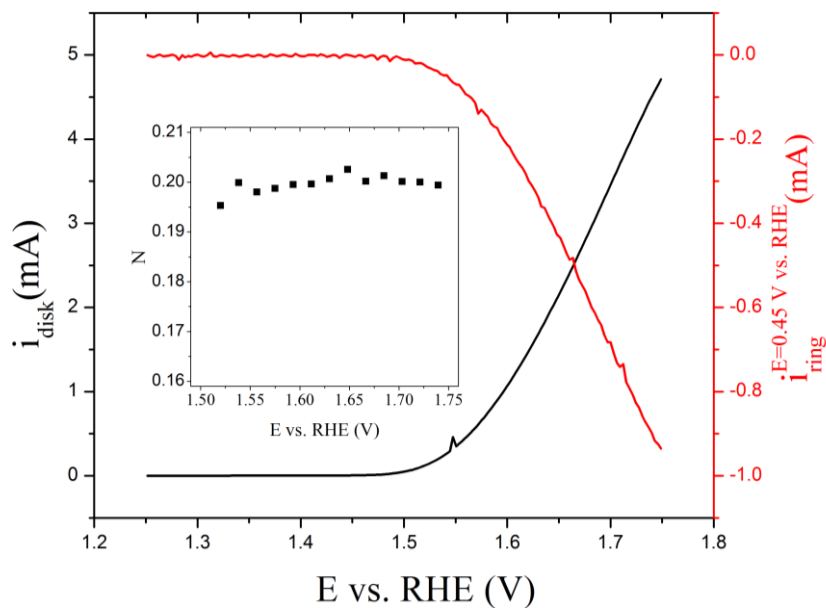
The faradaic efficiency towards water splitting in acid media was measured in RRDE configuration; the results are summarized in Figure E20. The efficiency ( $\epsilon$ ) was calculated with equation (D1), assuming that the oxygen reduction proceeds via four electron transfer, to produce water<sup>22</sup>.

$$\epsilon = \frac{i_{ring}}{i_{disk} \cdot N} \times 100 \quad (E1)$$

The collection factor (N) for oxygen was measured by using IrO<sub>2</sub> as reference catalyst (see Figure E21 for further details), and the value obtained was  $0.199 \pm 0.001$ , which corresponds well with the value obtained from measurements with the redox couple [Fe(CN)<sub>6</sub>]<sup>3-</sup>/[Fe(CN)<sub>6</sub>]<sup>4-</sup> (N=0.23); the small difference has been attributed to the non-ideal outward flow of O<sub>2</sub><sup>23</sup>.



**Figure E20.** RRDE measurement of the catalytic activity of Ba<sub>2</sub>PrIrO<sub>6</sub> towards water splitting in 0.1 M HClO<sub>4</sub>; measurements were performed by cyclic voltammetry at 0.01 V/s. Insert: Faradaic efficiency for water splitting.

Collection factor for O<sub>2</sub> detections in the RRDE configuration

**Figure E21.** Oxygen collection factor measurement. Scan rate: 0.01 V/s, rotation rate: 1500 RPM.

The collection factor was measured assuming that oxygen is reduced to water ( $\text{O}_2 + 4\text{H}^+ + 4\text{e}^- \rightarrow 2\text{H}_2\text{O}$ )<sup>22</sup>, according to the following equation<sup>24</sup>:

$$N = \frac{i_{\text{ring}}}{i_{\text{disk}}} \quad (\text{E2})$$

### Elemental analysis of the dissolved components from the Ba<sub>2</sub>PrIrO<sub>6</sub> double perovskite after electrochemical water oxidation at pH 1

The amount of dissolved components from the praseodymium-barium iridium double perovskite after electrochemical water oxidation experiments in 0.1 M HClO<sub>4</sub> was measured by means of inductively coupled plasma atomic emission spectroscopy (ICP-AES). These experiments were performed potentiostatically (1 h electrolysis) and in non-rotating conditions, using 10 mL of electrolyte. The double perovskite catalyst was drop-casted on a gold disk (950 μg<sub>oxide</sub>/cm<sub>disk</sub><sup>2</sup> of Ba<sub>2</sub>PrIrO<sub>6</sub>), using the ethanol-based ink similar to the one described for the RRDE experiments but with higher perovskite content (30 mg<sub>oxide</sub>/mL<sub>ink</sub>). The electrolyte was analyzed directly in a Varian Vista-MPX CCD Simultaneous ICP-AES. Table E3 summarizes the ICP-AES results.

**Table E3.** Fraction of Ba, Pr and Ir dissolved from the Ba<sub>2</sub>PrIrO<sub>6</sub> after 1 h of electrolysis at constant potential in HClO<sub>4</sub> 0.1 M.

<b>E vs. RHE (V)</b>	<b>% Ba leached</b>	<b>% Ir leached</b>	<b>% Pr leached</b>
<b>1.45</b>	12.7	0.6	9.5
<b>1.55</b>	14.2	0.8	11.3

The fraction of dissolved metal (% M leached) was calculated as follows:

$$\% \text{ M leached} = \frac{m_M(\text{mg}) \text{ in solution}}{m_M(\text{mg}) \text{ drop - casted}} \times 100$$

In this equation  $m_M$  (mg) *in solution* was obtained from the ICP-AES analysis after the electrolysis experiment and  $m_M$  (mg)*drop-casted* corresponds to the mass of each component of the Ba<sub>2</sub>PrIrO<sub>6</sub> double perovskite, calculated from its stoichiometry.

The results in table E2 show that approximately 10% of Ba and Pr are leached out from the double perovskite in the potential region 1.45 – 1.55 V vs. RHE, however, the dissolution of the noble metal is negligible.

## REFERENCES

- (1) Fu, W. T.; Ijdo, D. J. W. *J. Solid State Chem.* 2005, 178, 1312.
- (2) Meyer, H. M.; Hill, D. M.; Wagener, T. J.; Gao, Y.; Weaver, J. H.; Capone, D. W.; Goretta, K. C. *Phys. Rev. B* 1988, 38, 6500.
- (3) Fukuda, Y.; Nagoshi, M.; Suzuki, T.; Namba, Y.; Syono, Y.; Tachiki, M. *Phys. Rev. B* 1989, 39, 11494.
- (4) Miot, C.; Husson, E.; Proust, C.; Erre, R.; Coutures, J. P. *J. Mater. Res.* 1997, 12, 2388.
- (5) Mukhopadhyay, S. M.; Chen, T. C. S. *J. Mater. Res.* 1995, 10, 1502.
- (6) Moulder, J. F.; Chastain, J. *Handbook of X-ray Photoelectron Spectroscopy: A Reference Book of Standard Spectra for Identification and Interpretation of XPS Data*; Physical Electronics, 1995.
- (7) Ogasawara, H.; Kotani, A.; Potze, R.; Sawatzky, G. A.; Thole, B. T. *Phys. Rev. B* 1991, 44, 5465.
- (8) Burroughs, P.; Hamnett, A.; Orchard, A. F.; Thornton, G. *J. Chem. Soc., Dalton Trans.* 1976, 1686.
- (9) Sarma, D. D.; Rao, C. N. R. *J. Electron. Spectrosc. Relat. Phenom.* 1980, 20, 25.
- (10) Kruczek, M.; Talik, E.; Pawlak, D. A.; Kołodziejak, K.; Łukasiewicz, T. *J. Alloys Compd.* 2007, 442, 255.
- (11) Lutkehoff, S.; Neumann, M.; Slebarski, A. *Phys. Rev. B* 1995, 52, 13808.
- (12) Berthou, H.; Jørgensen, C. K.; Bonnelle, C. *Chem. Phys. Lett.* 1976, 38, 199.

- (13) Felner, I.; Yeshurun, Y.; Hilscher, G.; Holubar, T.; Schaudy, G.; Yaron, U.; Cohen, O.; Wolfus, Y.; Yacoby, E. R.; Klein, L.; Potter, F. H.; Rastomjee, C. S.; Egdell, R. G. *Phys. Rev. B* 1992, *46*, 9132.
- (14) Atanasoska, L.; Atanasoski, R.; Trasatti, S. *Vacuum* 1990, *40*, 91.
- (15) Peuckert, M. *Surf. Sci.* 1984, *144*, 451.
- (16) Wertheim, G. K.; Guggenheim, H. J. *Phys. Rev. B* 1980, *22*, 4680.
- (17) Kötzt, R.; Neff, H.; Stucki, S. *J. Electrochem. Soc.* 1984, *131*, 72.
- (18) Hara, M.; Asami, K.; Hashimoto, K.; Masumoto, T. *Electrochim. Acta* 1983, *28*, 1073.
- (19) Fissel, A.; Dąbrowski, J.; Osten, H. J. *J. Appl. Phys.* 2002, *91*, 8986.
- (20) Hall, H. Y.; Sherwood, P. M. A. *Journal of the Chemical Society, Faraday Transactions 1: Physical Chemistry in Condensed Phases* 1984, *80*, 135.
- (21) Majjane, A.; Chahine, A.; Et-tabirou, M.; Echchahed, B.; Do, T.-O.; Breen, P. M. *Mater. Chem. Phys.* 2014, *143*, 779.
- (22) Marković, N. M.; Schmidt, T. J.; Stamenković, V.; Ross, P. N. *Fuel Cells* 2001, *1*, 105.
- (23) Lee, Y.; Suntivich, J.; May, K. J.; Perry, E. E.; Shao-Horn, Y. *The Journal of Physical Chemistry Letters* 2012, *3*, 399.
- (24) Bard Allen J., F. L. R. *Electrochemical Methods: Fundamentals and Applications*; 2nd ed., 2001.